Title
Tracking the motion of the KV1.2 voltage sensor reveals the molecular perturbations caused by a de novo mutation in a case of epilepsy

Authors
Pantazis, Antonios
Kaneko, Maki
Angelini, Marina
et al.

Tracking the motion of the K$_V$1.2 voltage sensor reveals the molecular perturbations caused by a *de novo* mutation in a case of epilepsy

Antonios Pantazis[1,2,3], **Maki Kaneko**[4,5], **Marina Angelini**[1], **Federica Steccanella**[1], **Annie M. Westerlund**[6], **Sarah H. Lindström**[2], **Michelle Nilsson**[2], **Lucie Delemotte**[6], **Sulagna C. Saitta**[7], **Riccardo Olcese**[1,8,9]

[1]Division of Molecular Medicine, Department of Anesthesiology & Perioperative Medicine, David Geffen School of Medicine, University of California at Los Angeles, Los Angeles, CA, USA

[2]Division of Neurobiology, Department of Biomedical and Clinical Sciences (BKV), Linköping University, Linköping, Sweden

[3]Wallenberg Center for Molecular Medicine, Linköping University, Linköping, Sweden

[4]Center for Personalized Medicine, Children's Hospital, Los Angeles, Los Angeles, CA, USA

[5]Division of Genomic Medicine, Department of Pathology, Children's Hospital Los Angeles, Los Angeles, CA, USA

[6]Science for Life Laboratory, Department of Applied Physics, KTH Royal Institute of Technology, Solna, Sweden

[7]Department of Obstetrics and Gynecology and Division of Medical Genetics, Department of Pediatrics, David Geffen School of Medicine, University of California at Los Angeles, Los Angeles, CA, USA

[8]Department of Physiology, David Geffen School of Medicine, University of California at Los Angeles, Los Angeles, CA, USA

[9]Brain Research Institute, David Geffen School of Medicine, University of California at Los Angeles, Los Angeles, CA, USA

Corresponding authors R. Olcese: Division of Molecular Medicine, Department of Anesthesiology & Perioperative Medicine, David Geffen School of Medicine, University of California at Los Angeles, 100 Stein Plaza, Los Angeles, CA 90095, USA; and A. Pantazis: Linköping University, Department of Biomedical & Clinical Sciences (BKV), SE-581 83 Linköping, Sweden. rolcese@ucla.edu or antonios.pantazis@liu.se.

Abstract

An exome-based diagnostic panel in an infant with epilepsy revealed a previously unreported *de novo* missense variant in *KCNA2*, which encodes voltage-gated K$^+$ channel K$_V$1.2. This variant causes substitution F302L, in helix S4 of the K$_V$1.2 voltage-sensing domain (VSD). F302L does not affect KCNA2 subunit membrane trafficking. However, it does alter channel functional properties, accelerating channel opening at more hyperpolarized membrane potentials, indicating gain of function. F302L also caused loss of K$_V$1.2 function via accelerated inactivation onset, decelerated recovery and shifted inactivation voltage dependence to more negative potentials. These effects, which are not fully rescued by coexpression of wild-type and mutant KCNA2 subunits, probably result from the enhancement of VSD function, as demonstrated by optically tracking VSD depolarization-evoked conformational rearrangements. In turn, molecular dynamics simulations suggest altered VSD exposure to membrane lipids. Compared to other encephalopathy patients with *KCNA2* mutations, the proband exhibits mild neurological impairment, more characteristic of patients with *KCNA2* loss of function. Based on this information, we propose a mechanism of epileptogenesis based on enhanced K$_V$1.2 inactivation leading to increased synaptic release preferentially in excitatory neurons, and hence the perturbation of the excitatory/inhibitory balance of neuronal circuits.

Keywords

Introduction

Voltage-dependent, potassium-selective K$_V$1.2 channels are homotetrameric proteins composed of KCNA2 subunits (Stuhmer et al. 1989; Long et al. 2005). *KCNA2* gene expression is localized in the distal axon initial segment and the juxtaparanodes, neighbouring the nodes of Ranvier, of both central and peripheral neurons (Rasband et al. 1998; Lorincz & Nusser, 2008; Vacher et al. 2008; Trimmer, 2015). In addition to K$_V$1.2 channels, KCNA2 subunits can co-assemble into heterotetrameric K$^+$ channels, for example with KCNA1 and KCNA4 (Sheng et al. 1993; Wang et al. 1993). These channels contribute to the delay, or D-type current (Storm, 1990), regulating action potential generation and neurotransmitter release (Debanne et al. 1997; Lambe & Aghajanian, 2001; Bean, 2007; Guan et al. 2007). Studies in both excitatory (Kole et al. 2007) and inhibitory (Rowan et al. 2014) neurons have demonstrated that K$_V$1 channels play a critical role in repolarizing the action potential generated at the axon initial segment and thus determine action potential duration.

Ion channel dysfunction can often cause serious disease (Ashcroft, 2000). Consistent with this critical role in neurobiology, *KCNA2* knock-out mice exhibited hyperexcitability and an epileptic phenotype (Brew et al. 2007). Also in the mouse, a laboratory-generated missense variant that reduced K$_V$1.2 functional expression resulted in cerebellar ataxia (Xie et al. 2010). In humans, the first *KCNA2* variant associated with epileptic encephalopathy was only recently reported (Pena & Coimbra, 2015), but the list is growing and by now both

gain- and loss-of-function mutations have been found to be associated with epilepsy and other neurological disorders (Pena & Coimbra, 2015; Syrbe et al. 2015; Allen et al. 2016; Corbett et al. 2016; Hundallah et al. 2016; Masnada et al. 2017).

In this work, we report a new variant of *KCNA2* from an infant with epilepsy. The *de novo*, heterozygous, c.906T>G missense mutation (Fig. 1) results in a p.Phe302Leu (F302L) amino acid substitution, located in the S4 segment of the voltage-sensor domain (VSD) of the $K_V1.2$ channel. This location is of particular importance for voltage-dependent channel activation: segment S4 bears highly conserved, positively charged residues that sense changes in the electric field across the cell membrane (Fig. 2A-D). Thus, upon membrane depolarization, the positively charged residues are compelled to move outward through the electric field. This transition is then electromechanically coupled to the channel gate, facilitating its opening and subsequent ionic conduction (Tombola et al. 2006; Borjesson & Elinder, 2008; Chanda & Bezanilla, 2008; Tao et al. 2010; Blunck & Batulan, 2012; Jensen et al. 2012; Fernandez-Marino et al. 2018).

The amino acid sequence of S4, including F302, is conserved across a variety of vertebrate and invertebrate animals (Fig. 2E), as expected of the prominent role of this segment in voltage sensitivity. Substitution F302L is located between conserved arginine residues R300 and R303, which correspond to R3 and R4 in the canonical S4 charge nomenclature (Fig. 2D). Specifically in $K_V1.2$ channels, residues R294 (R1), R297 (R2), R300 (R3) and R303 (R4) contribute to the charge that senses and responds to changes in the membrane potential (Ishida et al. 2015). Since F302L is a conservative change between two hydrophobic amino acids, and both gain and loss of $K_V1.2$ function have been associated with epileptic encephalopathy (Masnada et al. 2017), functional characterization of the F302L variant was required for confirmation of its pathogenicity and potential identification of treatments specific to this variant. $K_V1.2$ channels exhibit a complex response to membrane depolarization, characterized as fast opening followed by a slower channel closure, called slow inactivation, which renders the channel unresponsive to further depolarization until spontaneous recovery (Suarez-Delgado et al. 2020). F302L may affect either, or both, facets of $K_V1.2$ regulation by the membrane potential, with probable differential effects on cellular excitability.

We evaluated the consequences of mutation F302L on the biosynthetic, biophysical and structural properties of heterologously expressed $K_V1.2$ channels using optical, electrophysiological and computational methods. We found that KCNA2-F302L subunits traffic normally to the cell membrane; however, $K_V1.2$-F302L channels open faster and require less membrane depolarization to open: a gain-of-function effect. $K_V1.2$-F302L channels also exhibit enhanced inactivation, manifested as a faster rate of inactivation onset at a more hyperpolarized membrane potential and slower recovery: a loss-of-function effect. Neither of these effects could be fully rescued by the coexpression of wild-type and mutant KCNA2 subunits, in agreement with the dominant effect of the mutation in the proband. Optical tracking of the voltage-sensing domain of the channel, where the substitution is located, showed that the $K_V1.2$-F302L VSD exhibits a hyperpolarized and steeper voltage-dependence. This effect is possibly based on an altered exposure of the VSD S4 helix to its lipid environment, as shown in molecular dynamics simulations. We discuss that F302L may

alter $K_V1.2$ channel biophysical properties by enhancing VSD activation and its coupling to channel opening.

Methods

Ethical approval

Written informed consent was obtained from the patient's legal guardian for the publication of this case report. All animal protocols were approved by the UCLA Institutional Animal Care and Use Committee and conformed to the Guide for the Care and Use of Laboratory Animals published by the US National Institutes of Health. UCLA's animal care and use programme has been fully accredited by the Association for Assessment and Accreditation of Laboratory Animal Care International continuously since 1976. Oocytes were ethically collected from mature (9+ cm) female *Xenopus laevis* frogs (LM00535, Nasco). Frogs were housed in the UCLA Division for Laboratory Animal Service frog facility. Room temperature: 16–21°C; humidity: 37%; light cycle: 06.00–18.00 h. Water used in frog tanks was filtered continuously. Frogs were fed with frog brittle (Nasco) three times per week (Monday, Wednesday, Friday). Tanks were flushed daily. Filters were checked weekly and changed if needed. Carbon filters were changed monthly. Ovaries were collected after euthanasia. The animals were killed humanely by CNS pithing under full anaesthesia. Full anaesthesia was achieved by immersion in 0.17% tricaine, pH 7, for 40 min, ascertained by toe pinching. The investigators understand the ethical principles under which *The Journal of Physiology* operates and our work complies with the animal ethics checklist (Grundy, 2015).

Epilepsy panel

DNA was extracted from the peripheral blood of the patient and each of her unaffected parents as comparators using a commercially available kit (Promega Maxwell RSC DNA Extraction Kit, Madison, WI, USA). The exome sequencing library was generated for proband DNA using the Agilent SureSelect Human All Exon V6+Mito kit (Santa Clara, CA, USA). Captured DNA fragments were then sequenced using the Illumina Nextseq 500 sequencing system, with 2×100 bp paired-end reads. Single nucleotide variants (SNVs) and small insertions and deletions (<10 bp) were detected by mapping and comparing the DNA sequences with the human reference genome (GRCh37-hg19). Of all the variants identified by exome sequencing, a list of rare variants (minor allele frequency <1%) located within a predefined set of 166 epilepsy-associated genes (see below) was generated. These variants were further annotated and analysed using a commercial tool (Cartagenia v4.2). Only clinically significant or potentially significant variants were confirmed by Sanger sequencing and reported. The genes included in this panel are known to be associated with primary epilepsy, or associated with syndromes in which epilepsy is a commonly observed feature. The following genes were evaluated for sequence changes and small indels. For each gene the percentage of the coding region covered at a minimum of $10 \times$ is provided in parentheses:

ABAT (100), ADGRG1 (100), ADGRV1 (100), ADRA2B (100), ADSL (100), AFG3L2 (99.8), AKT3 (100), ALG13 (99.07), ARFGEF2 (100), ARHGEF9 (100), ASAH1 (100), ASPM (100), ATP1A2 (100), BCKDK (100), C12orf57 (100), CACNA1A (99.95),

*CACNA1H (99.77), CACNB4 (100), CASK (100), CASR (100), CDK5RAP2 (100),
CHD2 (100), CHRNA2 (100), CHRNA4 (100), CHRNA7 (100), CHRNB2 (100), CLCN2
(100), CLN3 (100), CLN5 (100), CLN6 (100), CLN8 (100), CNTNAP2 (100), COL4A1
(100), CPA6 (100), CSTB (100), CTSD (100), CUL4B (100), DCX (100), DEPDC5
(100), DNAJC5 (100), DNM1 (100), DOCK7 (100), DYNC1H1(100), DYRK1A (100),
EEF1A2 (100), EFHC1 (100), EPM2A (90.56), EXOSC3 (100), FIG4 (100), FLNA
(100), FOXG1(100), GABRA1(100), GABRB3(100), GABRG2 (98.85), GAMT (100),
GATM (100), GLI2 (100), GNAO1(100), GOSR2 (100), GPHN (100), GRIK2 (100),
GRIN1 (100),GRIN2A (100), GRIN2B (100), GRN(100), HCN1 (100), HNRNPU (100),
IER3IP1 (100), IQSEC2 (98.61), JRK (100), KANSL1 (100),* **KCNA2** *(100), KCNC1
(100), KCNH5 (100), KCNJ10 (100), KCNMA1 (100), KCTD7 (100), KPNA7 (100),
KPTN (100), LGI1 (100), LIAS (100), MAGI2 (97.17), MBD5 (100), MCPH1 (100),
MFSD8 (100), MTOR (100), NDE1 (100), NEDD4L (100), NHLRC (100), NRXN1 (100),
OPHN1 (100), PAFAH1B1 (100), PHF6 (100), PIGA (100), PIGN (100), PIGO (100),
PIGT (100), PLCB1 (100), PNKP (100), PPT1 (100), PRICKLE1 (100), PRICKLE2 (100),
PRRT2 (100), PTCH1 (100), PURA (100), QARS (100), ROGDI (100), SCARB2 (100),
SCN3A (100), SCN9A (99.9), SERPINI1 (100), SHANK3 (98.46), SHH(100), SIX3 (100),
SLC12A5 (100), SLC13A5 (100), SLC19A3 (99.94), SLC1A2 (100), SLC1A3 (100),
SLC25A12 (100), SLC25A22 (100), SLC35A2 (100), SLC35A3 (100), SLC9A6 (100),
SRPX2 (100), ST3GAL3 (100), ST3GAL5 (93.19), STX1B (100), STXBP1 (100), SYN1
(100), SYNGAP1 (98.18), SZT2 (100), TBC1D24 (100), TCF4 (100), TNK2 (99.7), TPP1
(100), TSC1 (100), TSC2 (100), TSEN2 (100), TSEN54 (96.1), TUBA1A (100), TUBB2A
(100), UBE3A (100), WDR45 (100), WDR62 (100), WWOX (100)* and *ZEB2 (100).*

S4 amino acid sequence alignment of *KCNA2* orthologues

KCNA2 orthologues were identified by Basic Local Alignment Search Tool (BLAST)'s
Protein BLAST function (Altschul et al. 1990) using human *KCNA2* amino acid sequence
(accession: NP_004965.1) as the query sequence. Alignments of the S4 region were
generated using CLUSTAL Omega (Goujon et al. 2010; Sievers et al. 2011). The
following proteins were used in the alignment: human (*Homo sapiens*) NP_004965.1;
chimp (*Pan troglodytes*) XP_001162925.1, rat (*Rattus norvegicus*) NP_037102.1;
mouse (*Mus musculus*) NP_032443.3; rabbit (*Oryctolagus cuniculus*) NP_001076191.1;
dog (*Canis lupus familiaris*) XP_005621364.1; cow (*Bos taurus*) XP_005204216.1;
armadillo (*Dasypus novemcinctus*) XP_004484076.1; opossum (*Monodelphis domestica*)
XP_007485179.1; platypus (*Ornithorhynchus anatinus*) XP.028925757.1; chicken (*Gallus
gallus*) NP_989794.1; western clawed frog (*Xenopus tropicalis*) XP.031752644.1;
pufferfish (*Takifugu rubripes*) XP.003973122.1; zebrafish (*Danio rerio*) NP_001104640.1;
fruitfly (*Drosophila melanogaster*) NP_728123.1; nematode (*Caenorhabditis elegans*)
NP_001040829.1.

Immunocytochemistry and flow cytometry

Molecular biology.—A construct containing rat *KCNA2* with an N-terminally fused
enhanced green fluorescent protein (EGFP) tag (in the pEGFP-C1 vector) and an
extracellular haemagglutinin (HA) site (between transmembrane helices S1 and S2) was
a generous gift from Lily Jan and has been described previously (Gu et al. 2003). Using

this template, we constructed the EGFP-KCNA2(HA,F302L) plasmid via site-directed mutagenesis with a high-fidelity *Pfu* DNA polymerase (Agilent 600850) and confirmed by sequencing. A control plasmid carrying EGFP without KCNA2 was made as follows: first, a *Bgl*II site was introduced after the KCNA2(HA) sequence by site-directed mutagenesis, resulting in the KCNA2(HA) open reading frame (ORF) being flanked by *Bgl*II sites. The KCNA2(HA) sequence was then excised by *Bgl*II digestion, and the pEGFP-C1 vector was isolated by gel extraction, recircularized by T4 ligase and amplified.

COS-7 cell culture and transfection.—COS-7 cells (ECACC 87021302) were grown in Complete Culture Medium containing: Dulbecco's modified Eagle's medium (DMEM)/ F-12 Nutrient Mixture (1:1) (Gibco, Houston, TX, USA), heat-inactivated fetal bovine serum (FBS) (10%), penicillin (100 units), streptomycin (100 mg ml^{-1}) and glutamine (0.5 mM). Cultures were incubated at 37°C with 5% CO_2 and passaged twice per week up to p-24. Cells that would be used for flow cytometry (FC) were seeded in 12-well plates (~30,000 cells per well). Cells used for immunocytochemistry (ICC) were seeded in 35 mm glass-bottom dishes (~15,000 cells per dish). Transient transfection was done 24 h after seeding using TransIT-X2 Dynamic Delivery System (Mirus, Madison, WI, USA) according to the manufacturer. Briefly, plasmid DNA was mixed with unsupplemented DMEM/F-12 media (1 μg/103 μl for FC; 0.6 μg/250 μl for ICC). TransIT-X2 was added at a ratio of 4:1 (μl TransIT-X2: μg DNA) for FC or 2:1 for ICC and mixed by gentle pipetting. The mixture was incubated at room temperature for 25–30 min, to allow formation of TransIT-X2:DNA complexes. TransIT-X2:DNA complexes were added drop-wise to dishes containing cultured cells (60–80% confluent) and Complete Culture Medium. Before returning to the incubator, dishes were rocked gently to evenly distribute the TransIT-X2:DNA complexes. Culture medium was completely exchanged 24 h after transfection.

Immunocytochemistry/confocal microscopy.

At 48 h after transfection, glass-bottom culture dishes were rinsed three times, briefly, with ice-chilled Dulbecco's PBS supplemented with 0.9 mM Ca^{2+} and 0.5 mM Mg^{2+} (Gibco 14040-094). Cells were fixed for 5 min with 2 ml per dish of ice-chilled 4% paraformaldehyde in Ca^{2+}/Mg^{2+}-free PBS (Medicago 09-2051-100) and washed with PBS (once quickly, then 3×5 min each) before incubation with blocking solution (2 ml of 5% normal goat serum in PBS) for at least 1 h at room temperature. Primary (Rat anti-HA; Roche Cat. No. 3F10, RRID:AB_2314622, Indianapolis, IN, USA) and secondary (AlexaFluor 568 conjugated goat anti-rat IgG(H+L); Thermo Fisher Scientific Cat. No. A-11077, RRID:AB_2534121, Waltham, MA, USA) antibodies were diluted 1:200 and 1:1000, respectively, in blocking solution. The blocking solution was replaced with primary antibody solution (0.5 ml) and cells were incubated at room temperature for at least 2 h. Dishes were washed in PBS (1 ml each, 6×5 min) before incubation with secondary antibody solution (0.5 ml, 1 h at room temperature). Unbound antibodies were rinsed away with PBS (1 ml each, 3×10 min). After the final wash, excess PBS was carefully removed and a round coverslip was mounted over the glass-bottom of each dish using ProLong Glass Antifade Mountant (Invitrogen P36982, Carlsbad, CA, USA). Mountant was allowed to set for 18–24 h at room temperature, then samples were moved to 4°C for storage.

Confocal images were acquired using a Zeiss LSM 800 microscope with Zen 2.3 software in batches using identical fluorescence detection parameters across all samples. A z-stack was acquired for each cell (0.27 μm interval). For each cell, a final image was produced using Zen Image Analysis software to create an orthogonal projection of two consecutive z-sections where the cell had the largest cytoplasmic volume. Line profiles were drawn across each cell using Zen 3.0 Blue Edition software. Images were prepared for publication using Adobe Photoshop CS6. Identical adjustments to levels, sharpness and pixel sampling were performed on all images.

Flow cytometry.

To quantify KCNA2 subunit cell-surface expression, COS-7 cells were harvested by trypsinization (0.05%) 48 or 72 h after transfection. Thereafter, the cells were kept on ice in the dark unless otherwise stated. Cells were washed with ice-chilled Dulbecco's PBS (DPBS; Gibco) and pelleted at 400 g for 5 min at 4°C (Bourdin et al. 2016). To quantify surface channel expression in live cells, staining was performed sequentially with Zombie Violet viability dye (BioLegend, San Diego, CA, USA) and anti-HA-conjugated Alexa Fluor 647 (Alexa Fluor 647 anti-HA.11 Epitope Tag Antibody; BioLegend Cat. No. 682404, RRID:AB_2566616): first, cells were incubated in 100 μl Zombie Violet (1:500, PBS) for 15 min at room temperature; next, 100 μl ice-chilled 2× anti-HA647 (final concentration: 8 μg ml^{-1}, DPBS/5% FBS) was added. Samples were shaken for 45 min on ice at 250 rpm and washed in ice-chilled (i) DPBS/5% FBS and (ii) DPBS, as previously described (Bourdin et al. 2016). The optimal antibody and viability dye concentrations were determined by testing for best signal and least false-positives as in Bourdin et al. (2016). Finally, a single-cell suspension (300 μl DPBS) was prepared using pre-separation filters (Miltenyi Biotec, Bergisch Gladbach, Germany) (70 μm) and stored at 4°C in the dark.

Each measurement also included untransfected cells and cells transfected with EGFP alone, to calibrate the EGFP and anti-HA647 gates, respectively. FC was performed on the same day using a Gallios Flow Cytometer (Beckman Coulter Life Sciences, Indianapolis, IN, USA). Zombie Violet, EGFP and Anti-HA647 were excited at 405, 488 and 638 nm respectively.

Detection was filtered for wavelengths <480 nm using 450/50 nm, <550 nm with 525/40 nm and <710 nm with 660/20 nm. Counts of (i) cell clumps or cell fragments and (ii) dead cells were excluded using forward and side scatter gating (gate A), and Zombie Violet signal (gate B), respectively. Positive controls for Zombie Violet dye were generated by (i) permeabilizing and fixing cells using the eBioscience Foxp3/Transcription Factor Staining Buffer Set (Invitrogen) or (ii) incubation at 65 C for 1–10 min. Live cells were analysed for total channel expression (EGFP-positive cells, as compared to mock-transfected cells; gate C) and surface channel expression (anti-HA647-positive cells, as compared to unstained cells; gate D). Spillover of EGFP signal into the Zombie Violet-detecting channel was corrected by compensation at 1.4% using fluorescence-minus-one control.

Cells transfected with wild-type and mutant KCNA2 subunits were tested in triplicate from three different batches (passages 19–24) and at least 4000 live, EGFP-positive cells per replicate were counted at 30 μl min^{-1}. Data were analysed using Kaluza Analysis

1.3 (Beckman Coulter Life Sciences). Cell-surface expression was calculated as the fraction of anti-HA-positive cells in the EGFP-positive population, normalized to wild type KCNA2(HA) measurements. The difference in proportion of KCNA2-surface-positive COS-7 cells between KCNA2-WT and KCNA2-F302L was evaluated by Student's *t* test (two-tailed, equal variance). Error bars represent ±1 SEM, unless otherwise stated.

Electrophysiology and fluorometry

Molecular biology.—The rat *KCNA2* clone was used in the pMAX vector. Mutations F302L and/or A291C [for voltage clamp fluorometry (Horne et al. 2010); see below] were generated and confirmed by sequencing. The plasmid was linearized using *PacI* (New England Biolabs, Ipswich, MA, USA); cDNA (1 μg) was transcribed to cRNA *in vitro* (mMESSAGE MACHINE, Thermo Fisher Scientific) and stored at −80°C in RNA storage solution (Thermo Fisher Scientific).

Oocyte preparation.—*Xenopus laevis* (Nasco) oocytes (stages V–VI) were ethically isolated and defolliculated using standard procedures (Haug et al. 2004). The oocytes were injected with 50 nl of cRNA (0.1 ng nl^{-1}) using a Drummond nanoinjector. Injected oocytes were maintained at 18°C in an amphibian saline solution supplemented with 100 units ml^{-1} penicillin, 100 μg ml^{-1} streptomycin and 50 μg ml^{-1} gentamicin (Thermo Fisher Scientific).

Electrophysiology.—We used the cut-open oocyte Vaseline gap (COVG), a low-noise, fast voltage clamp technique (Taglialatela et al. 1992; Stefani & Bezanilla, 1998; Pantazis & Olcese, 2019). The oocyte was placed in a triple-compartment Perspex chamber, with a diameter of 600 μm for the top and bottom apertures. The upper chamber isolated the oocyte's upper domus and maintained it under clamp. The middle chamber provided a guard shield by clamping the middle part of the oocyte to the same potential as the upper chamber. The bottom chamber injected current intracellularly, through the saponin-permeabilized part of the oocyte. For experiments at 33°C, the chambers were heated using a polyimide-film-insulated heater (Omega Engineering, Norwalk, CT, USA), and the following: external solution (mM): 120 sodium methanesulfonate (MES), 2–5 K-MES, 2 Ca(MES)$_2$, 10 Hepes (pH 7.0); internal solution (mM): 120 potassium glutamate, 10 Hepes (pH 7.0); intracellular micropipette solution (mM): 2700 Na-MES, 10 NaCl. Low access resistance to the oocyte interior was obtained by permeabilizing the oocyte with 0.1% saponin carried by the internal solution. Holding potential was −80 mV. For activation experiments, 100 ms pulses were used (−80, …, 80 mV) with V = 20 mV and inter-pulse duration of 10 s. For inactivation experiments, 1 min pulses to variable potential (−80, …, 60 mV, V = 20 mV) were preceded and followed by brief (200 ms) pulses to 40 mV. The inter-pulse duration was 5 min.

Voltage clamp fluorometry.—Twenty-four hours before experimentation, the oocyte solution was supplemented with DTT (200 μM) and EDTA (10 μM), to make Cys available for fluorophore labelling. On the day of experiments, oocytes were rinsed in DTT- and EDTA-free saline and stained for 5 min with 20 μM MTS-TAMRA fluorophore in a depolarizing solution (in mM: 120 K-MES, 2 Ca(MES)$_2$ and 10 Hepes, pH 7.0) on ice, in the dark, to label the introduced Cys (A291C). The oocytes were then rinsed in dye-free

saline before being mounted in the recording chamber. Fluorescence emission and ionic current were simultaneously measured from the same area of membrane isolated by the top chamber (Gandhi & Olcese, 2008; Pantazis & Olcese, 2019). The same electrophysiological apparatus and solutions were used as above. The optical setup consisted of a Zeiss Axioscope FS microscope with filters (Semrock Brightline) appropriate for rhodamine excitation and emission wavelengths. The light source was a 530 nm, 158 lm Luxeon Rebel LED. A TTL-triggered Uniblitz VS 25 shutter (Vincent Associates, Rochester, NY, USA) was mounted on the excitation lightpath. The objective (Olympus LUMPlanFl, 40×, water immersion) had a numerical aperture of 0.8 and a working distance of 3.3 mm, which left sufficient room for insertion of the microelectrode while fully covering the oocyte domus exposed in the external recording chamber. The emission light was focused on a PIN-08-GL photodiode (UDT Technologies, FL, USA). A Dagan Photomax 200 amplifier was used for the amplification of the photocurrent and background fluorescence subtraction.

Data analysis and modelling

Electrophysiological data analysis.: Steady-state activation was calculated by fitting the macroscopic conductance to a Boltzmann distribution:

$$G = \frac{G_{max}}{1 + \exp\left[\frac{zF}{RT}(V_{0.5} - V_m)\right]}$$

(1)

where V_m is the membrane potential; $V_{0.5}$ is the half-activation potential; z is the effective valence; F and R are Faraday and Gas constants, respectively; and T is temperature (294 K). The maximal macroscopic conductance, G, was calculated by dividing the current (I) by the driving force:

$$G = \frac{I}{V_m - E_K}$$

(2)

where E_K is the equilibrium potential for potassium.

To determine current kinetics, current traces were fit to the sum of two exponential functions:

$$I = b + \sum_{i=1}^{2} a_i \exp\left(-\frac{t}{\tau_i}\right)$$

(3)

The reported time constant is the weighted mean of the two exponential components:

$$\tau_{avg} = \frac{a_1\tau_1 + a_2\tau_2}{a_1 + a_2}$$

(4)

The voltage dependence of slow inactivation was calculated by fitting thefraction of non-inactivated current to a Boltzmann distribution:

$$\frac{I_{\text{post}}}{I_{\text{pre}}} = \frac{1 - p\,ed}{1 + \exp\left[-\frac{zF}{RT}(V_{0.5} - V_{\text{m}})\right]} + p\,ed \qquad (5)$$

where I_{pre} and I_{post} are the current (at +40 mV) before and after the inactivating pulse, respectively, and *ped* is the non-inactivating pedestal current.

Inactivation onset kinetics were characterized by fitting both the activation and the inactivation parts of the current to the sum of three exponential equations [same as eqn (3) with $i = 1, \ldots, 3$]. The first two exponential components fit inactivation ($a_1, a_2 > 0$) and the third activation ($a_3 < 0$). The reported inactivation time constant was the weighted average of the two inactivation components [same formula as in as eqn (4)].

To characterize inactivation recovery kinetics, the fraction of recovered current at different intervals at −80 mV after the inactivating pulse (1 min at −20 mV) were fit to the following bi-exponential function:

$$\frac{I_{post}}{I_{pre}} = b + (1 - b) \cdot \sum_{i=1}^{2} a_i \exp\left(-\frac{\tau_i}{t}\right) \qquad (6)$$

where $a_2 = 1 - a_1$. This function asymptotes at 1 (full recovery). Baseline offset b represented non-inactivated current, accounted for by the differential degrees of activation/inactivation of WT and F302L channels, at room temperature or 33°C, following a 1 min pulse at −20 mV.

The voltage dependence of fluorescence deflections (ΔF; i.e. VSD activation) was estimated by fitting ΔF to a Boltzmann distribution:

$$\Delta F = \frac{\Delta F_{\text{max}} - \Delta F_{\text{min}}}{1 + \exp\left[\frac{zF}{RT}(V_{0.5} - V_{\text{m}})\right]} + \Delta F_{\text{min}} \qquad (7)$$

where ΔF_{max} and ΔF_{min} are the maximal and minimal ΔF asymptotes, respectively.

All electrophysiological data analysis was performed by least squares fitting in Microsoft Excel.

Markov model construction and fitting—A 17-state Markov state model was constructed to account for the effects of F302L on $K_V 1.2$ VSD activation and channel opening (see Fig. 12). It was based on the 16-state model by Ledwell & Aldrich (1999) for *Shaker* K$^+$ channel gating, as also used by Ishida et al. (2015) to model $K_V 1.2$ gating, with the addition of a transition to an inactivated state. Each VSD in the model underwent two voltage-dependent activation transitions ($R_1 \leftrightarrow R_2$ and $R_2 \leftrightarrow A$), with forward rates α and γ, respectively, and backward rates β and δ, respectively. Activation of all four VSDs allowed a transition to the open state, with forward rate k_O and backward rate k_C, both voltage-independent. The open state was connected to a closed state representing the

inactivated channel, via voltage-dependent rates ε and ζ, representing onset and recovery from inactivation, respectively.

Each voltage-dependent rate constant was expressed according to Eyring theory, e.g:

$$\alpha = \alpha_0 \exp\left(\frac{z_\alpha F V_m}{RT}\right)$$

(8)

$$\beta = \beta_0 \exp\left(-\frac{z_\beta F V_m}{RT}\right)$$

(9)

for forward and backward rates, respectively, where α_0 and β_0 were the values of α and β at $V_m = 0$ mV and z_α and z_β were the equivalent charge movements up to the transition state for each transition.

Calculations for state occupancies and the rate constants were performed using the Q-matrix method (Colquhoun & Hawkes, 1977, 1982, 1995). Briefly, $\mathbf{Q}$ is an $n \times n$-element matrix, where n is the number of states (in this case 17) and each element $q_{i,j}$ is the rate constant for the transition from state i to state j. If there is no connection between states i and j then $q_{i,j} = 0$. Each diagonal element is the negative sum of the off-diagonal elements in its row. The transition rates are then given by:

$$\frac{d\mathbf{p}(t)}{dt} = \mathbf{p}(t)\mathbf{Q}$$

(10)

where $\mathbf{p}(t)$ is a 1×17 vector of probability (occupancy) for each state such that its sum is 1. It was calculated in Mathworks Matlab using the *ode15s* solver. The voltage steps for the model were simulated with a 30 μs time constant to reproduce the cut-open oocyte clamp time constant and help the differential equation solver by reducing stiffness. For initial conditions and background fluorescence calculations, the state occupancies at steady state were calculated using:

$$\mathbf{p}(\infty) = \mathbf{u}^T\left(\mathbf{S}\mathbf{S}^T\right)^{-1}$$

(11)

where $\mathbf{S}$ is $[\mathbf{Q}\ \mathbf{u}]$ and $\mathbf{u}$ is a 17×1 unit vector.

The macroscopic current was simulated by:

$$I(t) = p_O(t)\,G\,(V_m(t) - E_K)$$

(12)

where $p_O(t)$ is the occupancy of the open state, G is maximal macroscopic conductance and E_K is the reversal potential for K^+.

We used the following equation to simulate a fluorescence signal (F) from VSD transitions:

$$\Delta F(t) = \sum_{i=1}^{2} \mathbf{p}(t) \cdot \mathbf{n}_i \cdot \varphi_i - \sum_{i=1}^{2} \mathbf{p}_{-80}(\infty) \cdot \mathbf{n}_i \cdot \varphi_i \tag{13}$$

where φ_1 and φ_2 are free parameters representing the macroscopic changes in fluorescence for the $R_1 \rightarrow R_2$ and $R_2 \rightarrow A$ transitions, respectively; and $\mathbf{n}_1$, $\mathbf{n}_2$ are each 17×1 vectors with the number of VSDs in the R_2 or A conformation for each model state ($\mathbf{n}_1$) or the A conformation ($\mathbf{n}_2$), and divided by 4, the total number of VSDs. Because the fluorescence traces were bleach- and background-subtracted during a recording at the holding potential (−80 mV), the simulated fluorescence level at −80 mV was also subtracted from the model output: in the second term, $\mathbf{p}_{-80}(\infty)$ is a vector containing the steady-state occupancies at −80 mV, calculated using eqn (11).

Rate optimization was performed in Matlab by least squares and using *fminsearchbnd* (D'Errico, 2012).

Statistical analysis.—The difference in oocyte macroscopic conductance was evaluated by Student's *t* test (two-tailed, equal variance). Error bars represent ±1 SD, unless otherwise stated.

Molecular dynamics simulations

For both K_V1.2-WT and -F302L channels, we built one model each of the activated-open (AO) and the resting-closed (RC) state. The AO state was based on the K_V1.2-2.1 chimera crystal structure by the MacKinnon group (PDB: #2R9R) (Long et al. 2007); the RC conformation was extracted from a long simulation of the K_V1.2-2.1 chimera channel under hyperpolarizing conditions by the Shaw group (Jensen et al. 2012). Modelling was done using a sequence alignment of KCNA2 rat sequence and the K_V1.2-2.1 chimera. Rosetta (Leaver-Fay et al. 2011) was used to construct the homology models of K_V1.2. Each protein was inserted into a POPC membrane with 51,657 water molecules in the AO system (Fig. 2) and 50,732 water molecules in the RC system. Neutralizing ions corresponding to 150 mM KCl (140–142 mM Cl⁻ and 180–183 mM K⁺ ions) were also added to each system. The systems were built using CHARMM-GUI (Jo et al. 2008).

The simulations were performed using the CHARMM36 forcefield (Lee et al. 2016). Before launching production simulations, each system was equilibrated in an NVT ensemble for 50 ps with harmonic restraints on the position of protein atoms. Following this, the volume of the simulation box was relaxed while using a semi-isotropic coupling of the pressure. The position restraints on protein atoms were decreased incrementally for 325 ps.

For production, the systems were simulated in NPT ensembles with a 2 fs timestep, a pressure of 1 atm and semi-isotropic Parrinello–Rahman barostat (Parrinello & Rahman, 1981). The temperature was set to 303.15 K, and the Nose–Hoover thermostat (Nose, 1984) was used. All bonds including hydrogens were constrained with LINCS (Hess et al. 1997). Short-range electrostatics were modelled within a 1.2 nm cutoff, with a switching function starting from 1.0 nm. Long-range electrostatics were modelled with particle mesh Ewald

(Darden et al. 1993). The systems were simulated for ~700 ns. The analyses were carried out on the last 450 ns of each trajectory.

Water density was calculated on a 1 Å grid over the simulation box using Volmap in VMD (Humphrey et al. 1996). From this, the density along the Z-direction in the VSD was averaged over X, Y-values spanning the VSD volume. The reference was defined as the centre of mass of six reference residues located on S1–S3 (A162, T184, F223, R240, N256, E273).

Electrostatic potential was calculated on a 1 Å grid over the simulation box using PME potential in VMD (Humphrey et al. 1996). The negative gradient of the electrostatic potential in Z yielded the electric field (Roux, 2008). The Z-component of the electric field at the location of charged residues was reported.

The lipid density around each residue was calculated by counting lipid atoms within 4.5 Å of each residue heavy atom. P-values were calculated with a Student's t test.

Results

A new variant of KCNA2 is associated with epilepsy

The proband is a female infant with onset of generalized clonic seizures at age 5 months. She displayed clusters of seizures provoked by fever or overheating, overlapping with a Dravet phenotype (Wolff et al. 2006). EEGs performed at 9 and 13 months of age were normal. Developmentally, her first words were at 10 months, she walked at 14 months, and had more than 50 words and some two-word phrases at 2 years of age. There was mild ataxia while walking, but her fine motor coordination appeared normal at 2 years of age. As of 3.5 years, she spoke in three to five-word sentences and no ataxia was noted. While her walking was normal, running skills were immature. After molecular diagnosis, she was treated with topiramate, and has remained seizure free for at least 29 months.

Using an exome-based DNA panel of 166 epilepsy genes, a heterozygous c.906T>G missense change in the *KCNA2* (transcript: NM_004974.3) was identified. Subsequent targeted Sanger sequencing of peripheral blood DNA from the patient and both of her parents confirmed this as a *de novo* variant (Fig. 1). The c.906T>G missense variant has never been recorded in population databases such as the Genome Aggregation Database [gnomAD (Lek et al. 2016)] or the Exome Aggregation Consortium [ExAC (Lek et al. 2016)]. The variant has not been described in commonly used databases of clinically significant variants [ClinVar (Landrum et al. 2018) and the Human Gene Mutation Database (Stenson et al. 2017)]. No other pathogenic variants were found in the patient's analysis.

The resulting F302L amino acid substitution is predicted as deleterious (disease causing) by algorithms used to evaluate the effect of missense changes on protein structure and function [GVGD, Mutation Taster (Schwarz et al. 2014)]. This was not surprising, considering the sensitive location of F302 on the highly conserved S4 helix: a principal component of the channel voltage-sensing apparatus (Fig. 2). Moreover, the patient's initial semiology of

febrile seizures is consistent with some of the reported cases of *KCNA2*-related epilepsy (Masnada et al. 2017).

F302L does not affect KCNA2 subunit surface expression

While *KCNA2* variants with reduced macroscopic conductance have been previously reported (Masnada et al. 2017), there are no definitive reports of mutant KCNA2 subunits misfolding or failing to traffic to the membrane to date. However, it is not uncommon for pathogenic variants of other potassium channels to exhibit impaired membrane trafficking (Roden & Balser, 1999). We evaluated the biosynthesis and surface expression of KCNA2-F302L subunits using an EGFP-and-HA-tagged KCNA2 construct (Gu et al. 2003). The N-terminally fused EGFP provided a measure of total protein production. The HA tag, inserted at the extracellular KCNA2 loop between transmembrane helices S1 and S2, was only accessible for anti-HA immunolabelling from the exterior of non-permeabilized cells and therefore served as a marker for surface-expressed channels (Fig. 3A). Immunocytochemistry experiments showed both cytosolic and cell surface localization for both wild-type and F302L KCNA2 subunits (Fig. 3B).

To better quantify the proportion of cells expressing KCNA2 subunits on their surface, we performed FC using the same cells and constructs. We found that the same proportion of cells transfected with KCNA2-WT or -F302L subunits were positive for surface trafficking (Fig. 3C-E). Moreover, the intensity distribution for the anti-HA signal was practically identical for cells expressing KCNA2-WT or -F302L subunits (Fig. 3D), consistent with similar cellular expression levels. Taken together with the electrophysiology results below, these experiments show that F302L does not impair KCNA2 subunit membrane trafficking.

F302L facilitates $K_V1.2$ channel opening

To evaluate the effect of F302L on $K_V1.2$ channel function, we expressed WT or F302L $K_V1.2$ channels in *Xenopus* oocytes and characterized their electrophysiological properties using the COVG technique (Taglialatela et al. 1992; Stefani & Bezanilla, 1998; Pantazis & Olcese, 2019) (Fig. 4A). $K_V1.2$-F302L channels opened at more negative potentials than $K_V1.2$-WT ($V_{0.5} = -15$mV), although the effective valence of channel opening was slightly decreased, by ~11% (Fig. 4B). Combined, the effects on voltage dependence lead to increased channel opening within the range of –40 to 40 mV, well within physiologically relevant membrane potentials. In addition, the macroscopic kinetics of channel opening were accelerated, particularly at more negative potentials: at –20 mV, $K_V1.2$-F302L channels opened over twice as fast as the WT channels (Fig. 4C).

Coexpression of WT and F302L subunits (equimolar cRNA injection) resulted in a more moderate phenotype, with a voltage-dependence curve falling between that of WT and F302L homomeric channels ($V_{0.5} = -8$mV; Fig. 4B). The effective valence of these channels matched those of F302L homomers, while the activation kinetics were closer to those of WT channels (Fig. 4C). The inability of KCNA2-WT subunits to fully rescue the KCNA2-F302L electrophysiological properties is consistent with the dominant effect of the mutation in the proband.

We also observed that the maximal macroscopic conductance of oocytes expressing KCNA2-WT, KCNA2-F302L, or coexpressed WT and F302L subunits was not significantly different ($P > 0.4$ for either condition; Fig. 1D) so the mutation does not appear to perturb the functional trafficking of $K_V1.2$ channels in this expression system.

These effects of F302L (left-shifted voltage dependence and accelerated opening) were recapitulated in experiments performed at a more physiological temperature (33°C; Fig. 5).

F302L facilitates K$_V$1.2 channel inactivation

$K_V1.2$ channels exhibit slow inactivation during prolonged membrane depolarization (Sprunger et al. 1996; Suarez-Delgado et al. 2020). To evaluate the effect of F302L on this facet of $K_V1.2$ voltage-dependent regulation, we used the following voltage protocol on oocytes expressing $K_V1.2$-WT or -F302L channels and clamped using COVG: a 1 min pulse at potentials varying from −80 to +80 mV was used to bring about increasing occupancy of inactivation. Brief pulses immediately preceding and following the inactivation pulse (the pre- and post-pulses) were used to evaluate channel availability before and after inactivation (Fig. 6A). Mutation F302L shifted the voltage dependence of inactivation to more negative potentials ($V_{0.5} = −22$ mV) and mildly enhanced its apparent valence by 9% (Fig. 6B). Combined, these effects on the voltage dependence of slow inactivation means that $K_V1.2$-F302L channels begin to inactivate more by −40 mV, which could in turn reduce $K_V1.2$ current during sufficiently prolonged neuronal depolarization (Steriade et al. 1993). There did not appear to be a significant difference in the extent of inactivation, both channel types inactivating partially with ~20% pedestal (non-inactivating) current (Fig. 6B).

F302L also accelerated the onset of inactivation (Fig. 6C). This occurred at all potentials where $K_V1.2$ current could be detected until 40 mV, when the rates of inactivation matched across wild-type and F302L channels. At −20 mV, $K_V1.2$-F302L channels inactivated almost 3-fold faster than WT. This observation further adds to the premise that fewer $K_V1.2$-F302L channels would be available to produce current *in vivo*.

By varying the interval between the inactivating pulse and the brief post-pulse, we also evaluated the kinetics of inactivation recovery, which was slowed down in F302L (Fig. 6D). At −80 mV, inactivation recovery occurred with two kinetic components and, overall, $K_V1.2$-F302L channels were 2-fold slower to recover than WT.

As in the case of voltage-dependent activation, the coexpression of KCNA2-WT subunits tempered, but did not fully revert, the effect of F302L on the voltage dependence and kinetics of inactivation. In fact, the voltage dependence and kinetics of inactivation when KCNA2-WT and -F302L subunits were coexpressed more closely resembled those of homomeric $K_V1.2$-F302L channels: $V_{0.5} = −16$ mV; z higher by 5%; inactivation onset at −20 mV faster by ~2-fold; inactivation recovery at −80 mV slower by 1.8-fold (Fig. 6).

We were able to probe inactivation onset and recovery kinetics at a more physiological temperature (33°C), and the results recapitulate those from recordings at room temperature: faster onset of inactivation at −20 mV (Fig. 7A) and delayed recovery at −80 mV (Fig. 7).

F302L facilitates K$_V$1.2 VSD activation

Since the F302L substitution (i) is located in the S4 segment of the K$_V$1.2 channel voltage-sensing domain (Fig. 2) and (ii) affects the voltage-dependent operation of the channel (opening and inactivation; Figs 4-7), we posited that it must also alter the biophysical properties of the VSDs, because VSD conformational transitions are transduced into channel opening (Tombola et al. 2006; Blunck & Batulan, 2012; Jensen et al. 2012; Fernandez-Marino et al. 2018) and, by extension, slow inactivation (Conti et al. 2016; Suarez-Delgado et al. 2020). We optically tracked the activation transitions of the K$_V$1.2 VSD in conducting channels with or without F302L using voltage clamp fluorometry (Mannuzzu et al. 1996; Claydon & Fedida, 2007; Gandhi & Olcese, 2008; Blunck, 2015; Priest & Bezanilla, 2015; Cowgill & Chanda, 2019). By fluorescently labelling the VSD with a small, environment-sensitive probe, and complementing our electrophysiological set-up with epifluorescence capability, it was possible to simultaneously (i) control the membrane potential, (ii) record membrane current (i.e. channel opening) and (iii) acquire ensemble fluorescence, the deflections of which (F) reflect local protein conformational changes (Fig. 8). These experiments showed that the voltage dependence of K$_V$1.2-F302L VSD activation was also shifted to more negative potentials ($V_{0.5} = -4$ mV), and also acquired more sensitivity to changes in the membrane potential, as evidenced by more apparent valence, by 17%. We further discuss the relevance of these changes with respect to channel opening in the Discussion below.

F302L alters the environment of S4

To investigate molecular implications of the mutant, four homology models of the K$_V$1.2 channel were constructed. For both WT and F302L, we built one model each of the activated VSD – open pore (AO) and the resting VSD – closed pore (RC) states. A full simulation system consists of a protein in a membrane surrounded by water and neutralizing ions (Fig. 2B,C). We carried out 700 ns molecular simulations of the four systems.

The simulations predict that the F302L substitution changes neither the water content nor the electrostatic environment of the charged S4 residues (Fig. 9). A deeper interrogation of the structural differences between simulated K$_V$1.2 wild-type and F302L channels revealed that the mutation changes the lipid interactions of two S4 residues in the vicinity of position 302 in the AO state: L298 and I304. This alteration indicates a change of the S4 environment concomitant with a slight rotation of the S4 helix with respect to its surrounding transmembrane helices (Fig. 10). Together, these structural perturbations may account for the alteration of VSD functional properties (Fig. 8) and, consequently, K$_V$1.2 voltage-dependent operation (Figs 4-7).

Discussion

In this work, we report on a *KCNA2* variant discovered in a patient with epilepsy (Fig. 1). KCNA2 proteins are broadly expressed in the CNS, and assemble into homotetrameric, voltage-sensitive, potassium-selective K$_V$1.2 channels (Fig. 2). The resulting amino acid substitution, F302L, at the S4 transmembrane helix of the voltage-sensing domain (Fig. 2), does not seem to negatively affect subunit surface expression (Figs 3 and 4D). However, it

does affect the biophysical properties of $K_V1.2$ current, in both the absence and the presence of wild-type subunits. Both channel opening and slow inactivation are enhanced (Figs 4-7), producing both gain and loss of $K_V1.2$ function. We then optically tracked the activation of $K_V1.2$ voltage-sensing domains, where the F302L substitution is located, to discover that the mutation enhanced their voltage-sensing properties (Fig. 8). Finally, all-atom molecular dynamics simulations of $K_V1.2$ channels in two conformations showed F302L produces subtle, but detectable, structural perturbations: rotation of helix S4, and differential exposure of its residues to the membrane lipids (Fig. 10). Below, we discuss these results, to probe deeper into the molecular etiology of the perturbed electrophysiological properties of $K_V1.2$ channels; how these relate to neuronal macromolecular channel complexes, excitability and epileptogenesis; and how the advent of precision medicine can benefit from mechanistically rigorous biophysical studies.

A modest enhancement of the VSD voltage dependence accounts for augmented channel opening

Voltage-dependent channel opening emerges following the activation of specialized VSDs (Tombola et al. 2006; Borjesson & Elinder, 2008; Chanda & Bezanilla, 2008; Tao et al. 2010; Blunck & Batulan, 2012; Jensen et al. 2012; Fernandez-Marino et al. 2018). Voltage clamp fluorometry revealed that the VSDs of $K_V1.2$-F302L channels have a hyperpolarized half-activation potential and exhibit more sensitivity to changes in the membrane potential (Fig. 8). Compared to the effect on the voltage dependence of channel opening (Fig. 4B), the effect of F302L on VSD operation appears more modest. Plotting the 95% prediction bounds for the wild-type and F302L VSD activation probability shows that the two curves are clearly distinct, with the mutant VSD showing a steeper response to changes in the membrane potential (Fig. 11). Drawing on the basic operational principles of a tetrameric K^+ channel provides an interpretation for how a modest perturbation of VSD function translates to the larger effect observed in the channel conductance: because activation of all four VSDs is a necessary condition for pore opening (Schoppa et al. 1992; Bezanilla et al. 1994; Zagotta et al. 1994), a rough approximation of the channel open probability is the VSD activation probability raised to the fourth power. In Figure 11, the prediction bounds corresponding to VSD activation in $K_V1.2$-WT and -F302L channels were raised to the fourth power: the resulting curves are separated at their half-activation point ($V_{0.5}$) by ~10 mV, resembling the difference between $K_V1.2$-WT and -F302L channel-opening voltage dependence (Fig. 4B; $V_{0.5} = 15$ mV). In other words, the modest effect of mutation F302L on $K_V1.2$ VSD activation is consistent with the stronger shift observed in the voltage dependence of pore opening, when considering the basic operation of a homotetrameric K_V channel.

However, the above analysis does not account for other properties of $K_V1.2$-F302L channels, such as their accelerated activation kinetics (Fig. 4C) and the similarity in apparent valence of channel opening between F302L and WT channels (Fig. 4B). To address this evidence and reconcile voltage-sensor activation with channel opening in a more mechanistic manner, we simultaneously fit fluorescence and current data with a 17-state Markov state model of $K_V1.2$ voltage-dependent activation and inactivation (Fig. 12A). The model assumed a channel with four VSDs undergoing two sequential, voltage-dependent activation transitions

$(R_1 \leftrightarrow R_2 \leftrightarrow A)$, giving rise to 15 shut states. When all four VSDs are in the fully active (A) conformation, a voltage-independent transition led to the single open state. This model is inspired by those used by the Aldrich and Islas groups to characterize *Shaker* and K_V1.2 channel voltage-dependent activation (Ledwell & Aldrich, 1999; Ishida et al. 2015). Our variation included one more closed state, accessible via a voltage-dependent transition from the open state, representing the inactivated state. The model accounted for the enhanced opening of K_V1.2-F302L channels (Fig. 12B,C) by the combination of (at 0 mV): a 3.5-fold reduction of the first VSD activation transition; a 1.8-fold enhancement of the second VSD activation transition; and a 6.5-fold enhancement of the voltage-independent opening transition (Table 1). One interpretation of this result is that VSD activation in F302L channels is more effective at triggering pore opening than in the WT channel. The enhanced VSD activation is also consistent with facilitated inactivation, considering the interrelationship between the two processes shown in the related *Shaker* K^+ channel (Conti et al. 2016) and the similarity between *Shaker* C-type inactivation and the slow inactivation of K_V1.2 channels (Suarez-Delgado et al. 2020).

What is the structural basis for the effects of mutation F302L?

The location of the mutation on the S4 transmembrane helix (Fig. 2) and the alteration of the VSD activation properties (Figs 8 and 11) prompted us to query the structural basis for these effects, especially because the conservative nature of the F302L substitution precluded an immediate structure-based rationalization. Our molecular dynamics simulations did not reveal a gross alteration of the VSD hydration or electrostatic properties (Fig. 9). This is not surprising, considering that homologous VSDs from different channels exhibit little difference in these properties (Souza et al. 2014) and point to a more subtle structural effect of the conservative F302L substitution: while not providing a direct insight into the effect of the mutation, it lends weight to the validity of our computational simulations.

The differential exposure of residues L298 and I304 to membrane lipids is a statistically significant result encountered in all four VSDs of the modelled channels (Fig. 10C) and is in line with the alteration of hydrophobic surface area in the F302L substitution. Interaction with lipid is an important component of VSD operation (Sands & Sansom, 2007; Swartz, 2008; Milescu et al. 2009; Kasimova et al. 2014); together with the apparent rotation of the S4 helix with respect to its juxtaposed transmembrane helices, this effect could underlie the functional consequences of F302L on VSD operation, and K_V1.2 voltage-dependent properties.

KCNA2-F302L subunits in heteromeric K_V channel complexes

In this work, we studied the effects of amino acid substitution F302L in homomeric K_V1.2 channels. KCNA2 subunits can also assemble with related K_V pore-forming subunits into heterotetrameric voltage-dependent, K^+-selective channels (Isacoff et al. 1990; Ruppersberg et al. 1990; Sheng et al. 1993; Wang et al. 1993; Hopkins et al. 1994; Lai & Jan, 2006). K_V1.2 channels are also known to associate with accessory, cytoplasmic $K_V\beta2$ subunits *in vivo* (Rhodes et al. 1997). $K_V\beta2$ subunits bind to the cytosolic T1 domain of K_V1.2 channels (Long et al. 2005) and facilitate channel biosynthesis (Shi et al. 1996), while potentially conferring redox-sensitive gating properties (Long et al. 2005). Other proteins,

such as the amino acid transporter Slc7a5, have been reported to interact and modify the properties of $K_V1.2$ channels; in fact, this interaction seems to particularly exacerbate the electrophysiological properties of gain-of-function $K_V1.2$ mutants (Baronas et al. 2018). In this study, we focused on the properties of KCNA2-F302L subunits, alone or coexpressed with KCNA2-WT subunits. Certainly, delineating the effect of KCNA2-F302L subunits on, or in the presence of, known molecular associates will advance our understanding of the disease etiology. Given the dominant effect of KCNA2-F302L subunits on $K_V1.2$ current properties (Figs 4 and 6), we anticipate that the same will be observed in other macromolecular complexes where KCNA2-F302L subunits participate.

How do KCNA2-F302L subunits affect neuronal excitability?

How do these gating properties correlate with encephalopathy? Two potential means to address this question are (i) previous cases of *KCNA2*-related encephalopathies and (ii) studies on $K_V1.2$ channel expression and role in neuronal function.

Several *KCNA2* mutations with either gain, loss, or combined gain-and-loss-of-function have been reported in patients with epilepsy (Masnada et al. 2017). Their study reported that combined gain-and-loss-of-function mutations tend to result in earlier age of seizure onset (mean ~2 months as opposed to ~8 months for either gain- or loss-of-function); seizures that were more rarely triggered by fever; and cause more severe neurological phenotypes and more pronounced intellectual disability (Masnada et al. 2017). By comparison, the proband in our study exhibited febrile seizures with minor motor impairment and mild developmental delay. This difference could be due to the relatively minor effects of F302L on $K_V1.2$ functional properties, compared to gain-and-loss-of-function mutations reported in other probands. For instance, three patients with profound intellectual disability had variant T374A, which shifted $K_V1.2$ activation by ~−25 mV and decreased maximal conductance by ~7-fold (Masnada et al. 2017). As the patient in our study did not fully match the 'gain-and-loss-of-function' clinical phenotypes reported to date, do her symptoms align better with previous cases of encephalopathy with either gain or loss of *KCNA2* function? In general, patients with *KCNA2* gain of function have more severe clinical consequences than those with loss of function in terms of motor and intellectual impairment (Masnada et al. 2017). The relatively mild phenotype of the proband in this study suggests that *KCNA2* loss of function (enhanced inactivation) overall supersedes gain of function (facilitated opening) *in vivo*. In fact, the activation properties of currents recorded from oocytes expressing a mixture of KCNA2-WT and -F302L subunits were approximately half-way between homomeric $K_V1.2$-WT and -F302L channels (Fig. 4); their inactivation properties more closely approximated those of homomeric $K_V1.2$-F302L channels (Fig. 6).

The broad expression pattern of *KCNA2* in the CNS (Vacher et al. 2008) and the diversity of type, onset and severity for seizures in patients with different *KCNA2* mutations (Masnada et al. 2017) suggest that differential perturbations of $K_V1.2$ channel function promote epilepsy and other neurological disorders by diverse, probably non-mutually exclusive, mechanisms. Several mechanisms of how K_V (including $K_V1.2$) channel enhanced opening or inactivation can lead to epilepsy are discussed by Niday & Tzingounis (2018). We

propose an additional mechanism below, based on the role of $K_V1.2$ channels in setting action potential (AP) duration at the axon initial segment (AIS).

Long-lasting subthreshold depolarizations, such as cortical 'up states' (Steriade et al. 1993), could promote $K_V1.2$ inactivation: a process likely to be exacerbated by the enhanced inactivation properties of $K_V1.2$ channels containing KCNA2-F302L subunits (Figs 6 and 7). In cortical pyramidal (excitatory) neurons, AIS-localized K_V1 blockade or somatic current injections mimicking up-states produced broader APs, which propagated to the synapse and resulted in increased synaptic release (Kole et al. 2007). In contrast, AP broadening by AIS-localized K_V1 blockade in cerebellar stellate cells (inhibitory neurons) did not alter synaptic release (Rowan et al. 2014). This was due to the fast opening of K_V3 channels at presynaptic boutons, which locally restored AP duration (Rowan et al. 2014). Although the two cell types mentioned above participate in neuronal networks in different brain regions, these observations provide an example as to how enhanced $K_V1.2$ inactivation can differentially affect excitatory and inhibitory influences: a long-recognized mechanism of epileptogenesis (McCormick & Contreras, 2001). In fact, fast presynaptic K_V3 channels regulate interneuron synaptic release in several brain regions where epilepsy may arise, including the hippocampus (Lien & Jonas, 2003) and the cortex (Erisir et al. 1999; Rudy et al. 1999; Goldberg et al. 2005; Kaczmarek & Zhang, 2017). If the fast K_V3 channels at interneuron presynaptic terminals can largely correct aberrant AP duration due to K_V1 dysfunction at the AIS (Rowan et al. 2014), this may allot a higher contribution to *KCNA2*-mediated encephalopathy to excitatory neurons lacking axonal K_V3 channels.

In summary, (i) we found that F302L produces both gain- and loss-of-function effects on $K_V1.2$ channels; (ii) the proband has mild neurological symptoms, most consistent with cases of *KCNA2* loss of function, so enhanced $K_V1.2$ inactivation seems to be dominant *in vivo*; and (iii) loss of $K_V1.2$ function can produce broadened APs, leading to enhanced synaptic release preferentially in excitatory neurons, steering neuronal circuits towards epilepsy.

Potential therapeutic avenues

Functional characterization of a novel epilepsy-causing mutation can have impact on patient care in two ways: first, it confirms a functional effect, and hence, the pathogenicity of a novel variant, effectively ending a patient's diagnostic odyssey. Second, such a study may help to identify therapies specifically responsive to the functional effects of the mutation. At the time of our patient's initial genetic diagnosis, there were a few reports documenting favourable effects of acetazolamide on patients with *KCNA2*-related epilepsy (Pena & Coimbra, 2015; Allen et al. 2016). This prompted prescription of another carbonic anhydrase inhibitor, topiramate, to the patient at 13 months of age. Since then, the patient has been seizure-free for 29 months. While multiple mechanisms of actions for topiramate have been reported, it has been shown to enhance chloride currents of $GABA_A$ receptors with certain subunit combinations, and inhibit AMPA/kainate-evoked currents by allosterically affecting protein kinase A-mediated modulation of AMPAreceptors (Latini et al. 2008). Topiramate is also reported to increase brain GABA levels by NMR spectroscopy (Petroff et al. 2001; van Veenendaal et al. 2015). The effectiveness of topiramate for our

patient and its enhancing effects on GABAergic neurotransmission as well as inhibitory effects on glutamatergic neurotransmission are consistent with our proposed mechanism above, whereby F302L could promote epilepsy via unchecked excitatory signalling. Although the prescription of the medication preceded completion of our study in this case, it underlines the utility of our work for the identification of potential therapies specific to the disease-causing variant: the principle behind precision medicine.

A path for precision medicine, from molecules to the neuronal circuit

In this work, genetic screening in an infant patient with epilepsy revealed a previously unreported variant of the *KCNA2* gene, c.906T>G (Fig. 1). This missense mutation results in amino acid substitution F302L, at the primary structure of the *KCNA2* product, the pore-forming subunit of $K_V1.2$ channels (Fig. 2). Molecular dynamics simulations revealed that transmembrane helix S4, the secondary structural element of the KCNA2 subunit where F302L is located, is modestly rotated and exhibits differential interaction with membrane lipids compared to the WT helix (Fig. 10). S4 is a central component of the voltage-sensing domain, a conserved tertiary protein structure comprising a bundle of transmembrane helices that senses membrane depolarization. Optical investigations of this domain revealed that F302L results in a discernible enhancement of its depolarization-evoked conformational transitions (Figs 8 and 11). This modest effect was exacerbated in the $K_V1.2$ conduction properties, which emerge in the quaternary, tetrameric channel structure: interestingly, this conservative amino acid substitution resulted in both gain and loss of $K_V1.2$ function, manifested as facilitated voltage-dependent opening (Figs 4 and 5) and enhanced inactivation (Figs 6 and 7), respectively. Considering the mild symptoms of the patient, which better approximate those symptoms of patients with *KCNA2* loss-of-function reported to date (Masnada et al. 2017), we proposed that the enhanced inactivation effect of F302L outweighs gain-of-function due to facilitated opening *in vivo*. In turn, these results led us to propose a mechanism of epileptogenesis at the neuronal circuit level, whereby enhanced synaptic transmission by excitatory neurons perturbs the balance of excitatory and inhibitory activity, veering neuronal circuits towards synchronization and epilepsy. Next-generation sequencing of known epilepsy genes, either as part of a curated panel or through exome-based tests, has rapidly become part of the diagnostic approach towards epileptic disorders. Frequently, variants of uncertain significance are detected whose pathogenicity can remain unresolved without functional analysis. This study, starting with the detection of a nucleotide substitution and characterizing its effects through all levels of protein structure, to discussion of epileptogenesis at the neuronal network level, could set a paradigm for precision medicine-based approaches.

Data availability statement

The data that support the findings of this study are available from the corresponding authors upon reasonable request.

Supplementary Material

Refer to Web version on PubMed Central for supplementary material.

Biography

Antonios Pantazis: This project was Antonios' last at his previous position (UCLA; PI: Riccardo Olcese) and first at his first fully independent appointment, as Assistant Professor at Linköping University. He is particularly fond of this work because it combines highly diverse contributions from a truly international and multidisciplinary team of investigators, to address a case straight from the clinic. Antonios' research focus is on ion channel function and dysfunction. His team at LiU study how the intricate and dynamic structure of ion channels, their biophysical properties and their regulation relate to cellular excitability in health and, as in this article, disease.

References

Allen NM, Conroy J, Shahwan A, Lynch B, Correa RG, Pena SD, McCreary D, Magalhaes TR, Ennis S, Lynch SA & King MD (2016). Unexplained early onset epileptic encephalopathy: Exome screening and phenotype expansion. Epilepsia 57, e12–e17. [PubMed: 26648591]

Altschul SF, Gish W, Miller W, Myers EW & Lipman DJ (1990). Basic local alignment search tool. J Mol Biol 215, 403–410. [PubMed: 2231712]

Ashcroft FM (2000). Ion Channels and Disease. Elsevier, Oxford.

Baronas VA, Yang RY, Morales LC, Sipione S & Kurata HT (2018). Slc7a5 regulates Kv1.2 channels and modifies functional outcomes of epilepsy-linked channel mutations. Nat Commun 9, 4417. [PubMed: 30356053]

Bean BP (2007). The action potential in mammalian central neurons. Nat Rev Neurosci 8, 451–465. [PubMed: 17514198]

Bezanilla F, Perozo E & Stefani E (1994). Gating of Shaker K^+ channels: II. The components of gating currents and a model of channel activation. Biophys J 66, 1011–1021. [PubMed: 8038375]

Blunck R (2015). Investigation of ion channel structure using fluorescence spectroscopy. In Handbook of Ion Channels, ed. Zheng J & Trudeau MC, pp. 113–133. CRC Press, Boca Raton.

Blunck R & Batulan Z (2012). Mechanism of electromechanical coupling in voltage-gated potassium channels. Front Pharmacol 3, 166. [PubMed: 22988442]

Borjesson SI & Elinder F (2008). Structure, function, and modification of the voltage sensor in voltage-gated ion channels. Cell Biochem Biophys 52, 149–174. [PubMed: 18989792]

Bourdin B, Segura E, Tetreault MP, Lesage S & Parent L (2016). Determination of the relative cell surface and total expression of recombinant ion channels using flow cytometry. J Vis Exp 115, 54732.

Brew HM, Gittelman JX, Silverstein RS, Hanks TD, Demas VP, Robinson LC, Robbins CA, McKee-Johnson J, Chiu SY, Messing A & Tempel BL (2007). Seizures and reduced life span in mice lacking the potassium channel subunit Kv1.2, but hypoexcitability and enlarged Kv1 currents in auditory neurons. J Neurophysiol 98, 1501–1525. [PubMed: 17634333]

Chanda B & Bezanilla F (2008). A common pathway for charge transport through voltage-sensing domains. Neuron 57, 345–351. [PubMed: 18255028]

Claydon TW & Fedida D (2007). Voltage clamp fluorimetry studies of mammalian voltage-gated K^+ channel gating. Biochem Soc Trans 35, 1080–1082. [PubMed: 17956284]

Colquhoun D & Hawkes AG (1977). Relaxation and fluctuations of membrane currents that flow through drug-operated channels. Proc R Soc Lond B Biol Sci 199, 231–262. [PubMed: 22856]

Colquhoun D & Hawkes AG (1982). On the stochastic properties of bursts of single ion channel openings and of clusters of bursts. Philos Trans R Soc Lond B Biol Sci 300, 1–59. [PubMed: 6131450]

Colquhoun D & Hawkes AG (1995). A Q-matrix cookbook: how to write only one program to calculate the single-channel and macroscopic predictions for any kinetic mechanism. In Single Channel Recording, ed. Sakmann B & Neher E, 2nd edn, pp. 589–636. Plenum Press, New York.

Conti L, Renhorn J, Gabrielsson A, Turesson F, Liin SI, Lindahl E & Elinder F (2016). Reciprocal voltage sensor-to-pore coupling leads to potassium channel C-type inactivation. Sci Rep 6, 27562. [PubMed: 27278891]

Corbett MA, Bellows ST, Li M, Carroll R, Micallef S, Carvill GL, Myers CT, Howell KB, Maljevic S, Lerche H, Gazina EV, Mefford HC, Bahlo M, Berkovic SF, Petrou S, Scheffer IE & Gecz J (2016). Dominant KCNA2 mutation causes episodic ataxia and pharmacoresponsive epilepsy. Neurology 87, 1975–1984. [PubMed: 27733563]

Cowgill J & Chanda B (2019). The contribution of voltage clamp fluorometry to the understanding of channel and transporter mechanisms. J Gen Physiol 151, 1163–1172. [PubMed: 31431491]

D'Errico J (2020). fminsearchbnd, fminsearchcon MATLAB Central File Exchange. Retrieved September 10, 2020. https://www.mathworks.com/matlabcentral/fileexchange/8277-fminsearchbnd-fminsearchcon.

Darden T, York D & Pedersen L (1993). Particle mesh ewald - an N.Log(N) method for ewald sums in large systems. J Chem Phys 98, 10089–10092.

Debanne D, Guerineau NC, Gahwiler BH & Thompson SM (1997). Action-potential propagation gated by an axonal I(A)-like K^+ conductance in hippocampus. Nature 389, 286–289. [PubMed: 9305843]

Erisir A, Lau D, Rudy B & Leonard CS (1999). Function of specific K^+ channels in sustained high-frequency firing of fast-spiking neocortical interneurons. J Neurophysiol 82, 2476–2489. [PubMed: 10561420]

Fernandez-Marino AI, Harpole TJ, Oelstrom K, Delemotte L & Chanda B (2018). Gating interaction maps reveal a noncanonical electromechanical coupling mode in the Shaker K^+ channel. Nat Struct Mol Biol 25, 320–326. [PubMed: 29581567]

Gandhi CS & Olcese R (2008). The voltage-clamp fluorometry technique. Methods Mol Biol 491, 213–231. [PubMed: 18998096]

Goldberg EM, Watanabe S, Chang SY, Joho RH, Huang ZJ, Leonard CS & Rudy B (2005). Specific functions of synaptically localized potassium channels in synaptic transmission at the neocortical GABAergic fast-spiking cell synapse. J Neurosci 25, 5230–5235. [PubMed: 15917463]

Goujon M, McWilliam H, Li W, Valentin F, Squizzato S, Paern J & Lopez R (2010). A new bioinformatics analysis tools framework at EMBL-EBI. Nucleic Acids Res 38, W695–W699. [PubMed: 20439314]

Grundy D (2015). Principles and standards for reporting animal experiments in *The Journal of Physiology* and *Experimental Physiology*. J Physiol 593, 2547–2549. [PubMed: 26095019]

Gu C, Jan YN & Jan LY (2003). A conserved domain in axonal targeting of Kv1 (Shaker) voltage-gated potassium channels. Science 301, 646–649. [PubMed: 12893943]

Guan D, Lee JC, Higgs MH, Spain WJ & Foehring RC (2007). Functional roles of Kv1 channels in neocortical pyramidal neurons. J Neurophysiol 97, 1931–1940. [PubMed: 17215507]

Haug T, Sigg D, Ciani S, Toro L, Stefani E & Olcese R (2004). Regulation of K^+ flow by a ring of negative charges in the outer pore of BKCa channels. Part I: Aspartate 292 modulates K^+ conduction by external surface charge effect. J Gen Physiol 124, 173–184. [PubMed: 15277578]

Hess B, Bekker H, Berendsen HJC & Fraaije JGEM (1997). LINCS: a linear constraint solver for molecular simulations. J Comput Chem 18, 1463–1472.

Hopkins WF, Allen ML, Houamed KM & Tempel BL (1994). Properties of voltage-gated K^+ currents expressed in *Xenopus* oocytes by mKv1.1, mKv1.2 and their heteromultimers as revealed by mutagenesis of the dendrotoxin-binding site in mKv1.1. Pflugers Arch 428, 382–390. [PubMed: 7816560]

Horne AJ, Peters CJ, Claydon TW & Fedida D (2010). Fast and slow voltage sensor rearrangements during activation gating in Kv1.2 channels detected using tetramethylrhodamine fluorescence. J Gen Physiol 136, 83–99. [PubMed: 20584892]

Humphrey W, Dalke A & Schulten K (1996). VMD: visual molecular dynamics. J Mol Graph 14, 33–38, 27–38. [PubMed: 8744570]

Hundallah K, Alenizi A, AlHashem A & Tabarki B (2016). Severe early-onset epileptic encephalopathy due to mutations in the KCNA2 gene: Expansion of the genotypic and phenotypic spectrum. Eur J Paediatr Neurol 20, 657–660. [PubMed: 27117551]

Isacoff EY, Jan YN & Jan LY (1990). Evidence for the formation of heteromultimeric potassium channels in *Xenopus* oocytes. Nature 345, 530–534. [PubMed: 2112229]

Ishida IG, Rangel-Yescas GE, Carrasco-Zanini J & Islas LD (2015). Voltage-dependent gating and gating charge measurements in the Kv1.2 potassium channel. J Gen Physiol 145, 345–358. [PubMed: 25779871]

Jensen MO, Jogini V, Borhani DW, Leffler AE, Dror RO & Shaw DE (2012). Mechanism of voltage gating in potassium channels. Science 336, 229–233. [PubMed: 22499946]

Jo S, Kim T, Iyer VG & Im W (2008). CHARMM-GUI: a web-based graphical user interface for CHARMM. J Comput Chem 29, 1859–1865. [PubMed: 18351591]

Kaczmarek LK & Zhang Y (2017). Kv3 channels: enablers of rapid firing, neurotransmitter release, and neuronal endurance. Physiol Rev 97, 1431–1468. [PubMed: 28904001]

Kasimova MA, Tarek M, Shaytan AK, Shaitan KV & Delemotte L (2014). Voltage-gated ion channel modulation by lipids: insights from molecular dynamics simulations. Biochim Biophys Acta 1838, 1322–1331. [PubMed: 24513257]

Kole MH, Letzkus JJ & Stuart GJ (2007). Axon initial segment Kv1 channels control axonal action potential waveform and synaptic efficacy. Neuron 55, 633–647. [PubMed: 17698015]

Lai HC & Jan LY (2006). The distribution and targeting of neuronal voltage-gated ion channels. Nat Rev Neurosci 7, 548–562. [PubMed: 16791144]

Lambe EK & Aghajanian GK (2001). The role of Kv1.2-containing potassium channels in serotonin-induced glutamate release from thalamocortical terminals in rat frontal cortex. J Neurosci 21, 9955–9963. [PubMed: 11739602]

Landrum MJ, Lee JM, Benson M, Brown GR, Chao C, Chitipiralla S, Gu B, Hart J, Hoffman D, Jang W, Karapetyan K, Katz K, Liu C, Maddipatla Z, Malheiro A, McDaniel K, Ovetsky M, Riley G, Zhou G, Holmes JB, Kattman BL & Maglott DR (2018). ClinVar: improving access to variant interpretations and supporting evidence. Nucleic Acids Res 46, D1062–D1067. [PubMed: 29165669]

Latini G, Verrotti A, Manco R, Scardapane A, Del Vecchio A & Chiarelli F (2008). Topiramate: its pharmacological properties and therapeutic efficacy in epilepsy. Mini Rev Med Chem 8, 10–23. [PubMed: 18220981]

Leaver-Fay A, Tyka M, Lewis SM, Lange OF, Thompson J, Jacak R, Kaufman K, Renfrew PD, Smith CA, Sheffler W, Davis IW, Cooper S, Treuille A, Mandell DJ, Richter F, Ban YE, Fleishman SJ,

Corn JE, Kim DE, Lyskov S, Berrondo M, Mentzer S, Popovic Z, Havranek JJ, Karanicolas J, Das R, Meiler J, Kortemme T, Gray JJ, Kuhlman B, Baker D & Bradley P (2011). ROSETTA3: an object-oriented software suite for the simulation and design of macromolecules. Methods Enzymol 487, 545–574. [PubMed: 21187238]

Ledwell JL & Aldrich RW (1999). Mutations in the S4 region isolate the final voltage-dependent cooperative step in potassium channel activation. J Gen Physiol 113, 389–414. [PubMed: 10051516]

Lee J, Cheng X, Swails JM, Yeom MS, Eastman PK, Lemkul JA, Wei S, Buckner J, Jeong JC, Qi Y, Jo S, Pande VS, Case DA, Brooks CL 3rd, MacKerell AD Jr, Klauda JB & Im W (2016). CHARMM-GUI input generator for NAMD, GROMACS, AMBER, OpenMM, and CHARMM/OpenMM simulations using the CHARMM36 additive force field. J Chem Theory Comput 12, 405–413. [PubMed: 26631602]

Lek M, Karczewski KJ, Minikel EV, Samocha KE, Banks E, Fennell T, O'Donnell-Luria AH, Ware JS, Hill AJ, Cummings BB, Tukiainen T, Birnbaum DP, Kosmicki JA, Duncan LE, Estrada K, Zhao F, Zou J, Pierce-Hoffman E, Berghout J, Cooper DN, Deflaux N, DePristo M, Do R, Flannick J, Fromer M, Gauthier L, Goldstein J, Gupta N, Howrigan D, Kiezun A, Kurki MI, Moonshine AL, Natarajan P, Orozco L, Peloso GM, Poplin R, Rivas MA, Ruano-Rubio V, Rose SA, Ruderfer DM, Shakir K, Stenson PD, Stevens C, Thomas BP, Tiao G, Tusie-Luna MT, Weisburd B, Won HH, Yu D, Altshuler DM, Ardissino D, Boehnke M, Danesh J, Donnelly S, Elosua R, Florez JC, Gabriel SB, Getz G, Glatt SJ, Hultman CM, Kathiresan S, Laakso M, McCarroll S, McCarthy MI, McGovern D, McPherson R, Neale BM, Palotie A, Purcell SM, Saleheen D, Scharf JM, Sklar P, Sullivan PF, Tuomilehto J, Tsuang MT, Watkins HC, Wilson JG, Daly MJ & MacArthur DG & Exome Aggregation Consortium (2016). Analysis of protein-coding genetic variation in 60,706 humans. Nature 536, 285–291. [PubMed: 27535533]

Lien CC & Jonas P (2003). Kv3 potassium conductance is necessary and kinetically optimized for high-frequency action potential generation in hippocampal interneurons. J Neurosci 23, 2058–2068. [PubMed: 12657664]

Long SB, Campbell EB & Mackinnon R (2005). Crystal structure of a mammalian voltage-dependent Shaker family K$^+$ channel. Science 309, 897–903. [PubMed: 16002581]

Long SB, Tao X, Campbell EB & MacKinnon R (2007). Atomic structure of a voltage-dependent K$^+$ channel in a lipid membrane-like environment. Nature 450, 376–382. [PubMed: 18004376]

Lorincz A & Nusser Z (2008). Cell-type-dependent molecular composition of the axon initial segment. J Neurosci 28, 14329–14340. [PubMed: 19118165]

Mannuzzu LM, Moronne MM & Isacoff EY (1996). Direct physical measure of conformational rearrangement underlying potassium channel gating. Science 271, 213–216. [PubMed: 8539623]

Masnada S, Hedrich UBS, Gardella E, Schubert J, Kaiwar C, Klee EW, Lanpher BC, Gavrilova RH, Synofzik M, Bast T, Gorman K, King MD, Allen NM, Conroy J, Ben Zeev B, Tzadok M, Korff C, Dubois F, Ramsey K, Narayanan V, Serratosa JM, Giraldez BG, Helbig I, Marsh E, O'Brien M, Bergqvist CA, Binelli A, Porter B, Zaeyen E, Horovitz DD, Wolff M, Marjanovic D, Caglayan HS, Arslan M, Pena SDJ, Sisodiya SM, Balestrini S, Syrbe S, Veggiotti P, Lemke JR, Moller RS, Lerche H & Rubboli G (2017). Clinical spectrum and genotype-phenotype associations of KCNA2-related encephalopathies. Brain 140, 2337–2354. [PubMed: 29050392]

McCormick DA & Contreras D (2001). On the cellular and network bases of epileptic seizures. Annu Rev Physiol 63, 815–846. [PubMed: 11181977]

Milescu M, Bosmans F, Lee S, Alabi AA, Kim JI & Swartz KJ (2009). Interactions between lipids and voltage sensor paddles detected with tarantula toxins. Nat Struct Mol Biol 16, 1080–1085. [PubMed: 19783984]

Niday Z & Tzingounis AV (2018). Potassium channel gain of function in epilepsy: an unresolved paradox. Neuroscientist 24, 368–380. [PubMed: 29542386]

Nose S (1984). A unified formulation of the constant temperature molecular-dynamics methods. J Chem Phys 81, 511–519.

Pantazis A & Olcese R (2019). Cut-open oocyte voltage-clamp technique. In Encyclopedia of Biophysics, ed. Roberts G, Watts A & Societies EB, pp. 1–9. Springer, Berlin.

Parrinello M & Rahman A (1981). Polymorphic transitions in single-crystals – a new molecular-dynamics method. J Appl Phys 52, 7182–7190.

Pena SDJ & Coimbra RLM (2015). Ataxia and myoclonic epilepsy due to a heterozygous new mutation in KCNA2: proposal for a new channelopathy. Clin Genet 87, e1–e3. [PubMed: 25477152]

Petroff OA, Hyder F, Rothman DL & Mattson RH (2001). Topiramate rapidly raises brain GABA in epilepsy patients. Epilepsia 42, 543–548. [PubMed: 11440351]

Priest M & Bezanilla F (2015). Functional site-directed fluorometry. Adv Exp Med Biol 869, 55–76. [PubMed: 26381940]

Rasband MN, Trimmer JS, Schwarz TL, Levinson SR, Ellisman MH, Schachner M & Shrager P (1998). Potassium channel distribution, clustering, and function in remyelinating rat axons. J Neurosci 18, 36–47. [PubMed: 9412484]

Rhodes KJ, Strassle BW, Monaghan MM, Bekele-Arcuri Z, Matos MF & Trimmer JS (1997). Association and colocalization of the Kvβ1 and Kvβ2 β-subunits with Kv1 α-subunits in mammalian brain K$^+$ channel complexes. J Neurosci 17, 8246–8258. [PubMed: 9334400]

Roden DM & Balser JR (1999). A plethora of mechanisms in the HERG-related long QT syndrome. Genetics meets electrophysiology. Cardiovasc Res 44, 242–246. [PubMed: 10690299]

Roux B (2008). The membrane potential and its representation by a constant electric field in computer simulations. Biophys J 95, 4205–4216. [PubMed: 18641071]

Rowan MJ, Tranquil E & Christie JM (2014). Distinct Kv channel subtypes contribute to differences in spike signaling properties in the axon initial segment and presynaptic boutons of cerebellar interneurons. J Neurosci 34, 6611–6623. [PubMed: 24806686]

Rudy B, Chow A, Lau D, Amarillo Y, Ozaita A, Saganich M, Moreno H, Nadal MS, Hernandez-Pineda R, Hernandez-Cruz A, Erisir A, Leonard C & Vega-Saenz de Miera E (1999). Contributions of Kv3 channels to neuronal excitability. Ann N Y Acad Sci 868, 304–343. [PubMed: 10414303]

Ruppersberg JP, Schroter KH, Sakmann B, Stocker M, Sewing S & Pongs O (1990). Heteromultimeric channels formed by rat brain potassium-channel proteins. Nature 345, 535–537. [PubMed: 2348860]

Sands ZA & Sansom MS (2007). How does a voltage sensor interact with a lipid bilayer? Simulations of a potassium channel domain. Structure 15, 235–244. [PubMed: 17292841]

Schoppa NE, McCormack K, Tanouye MA & Sigworth FJ (1992). The size of gating charge in wild-type and mutant Shaker potassium channels. Science 255, 1712–1715. [PubMed: 1553560]

Schwarz JM, Cooper DN, Schuelke M & Seelow D (2014). MutationTaster2: mutation prediction for the deep-sequencing age. Nat Methods 11, 361–362. [PubMed: 24681721]

Sheng M, Liao YJ, Jan YN & Jan LY (1993). Presynaptic A-current based on heteromultimeric K$^+$ channels detected in vivo. Nature 365, 72–75. [PubMed: 8361540]

Shi G, Nakahira K, Hammond S, Rhodes KJ, Schechter LE & Trimmer JS (1996). Beta subunits promote K$^+$ channel surface expression through effects early in biosynthesis. Neuron 16, 843–852. [PubMed: 8608002]

Sievers F, Wilm A, Dineen D, Gibson TJ, Karplus K, Li W, Lopez R, McWilliam H, Remmert M, Soding J, Thompson JD & Higgins DG (2011). Fast, scalable generation of high-quality protein multiple sequence alignments using Clustal Omega. Mol Syst Biol 7, 539. [PubMed: 21988835]

Souza CS, Amaral C & Treptow W (2014). Electric fingerprint of voltage sensor domains. Proc Natl Acad Sci U S A 111, 17510–17515. [PubMed: 25422443]

Sprunger LK, Stewig NJ & O'Grady SM (1996). Effects of charybdotoxin on K$^+$ channel (KV1.2) deactivation and inactivation kinetics. Eur J Pharmacol 314, 357–364. [PubMed: 8957259]

Stefani E & Bezanilla F (1998). Cut-open oocyte voltage-clamp technique. Methods Enzymol 293, 300–318. [PubMed: 9711615]

Stenson PD, Mort M, Ball EV, Evans K, Hayden M, Heywood S, Hussain M, Phillips AD & Cooper DN (2017). The Human Gene Mutation Database: towards a comprehensive repository of inherited mutation data for medical research, genetic diagnosis and next-generation sequencing studies. Hum Genet 136, 665–677. [PubMed: 28349240]

Steriade M, Nunez A & Amzica F (1993). A novel slow (<1 Hz) oscillation of neocortical neurons in vivo: depolarizing and hyperpolarizing components. J Neurosci 13, 3252–3265. [PubMed: 8340806]

Storm JF (1990). Potassium currents in hippocampal pyramidal cells. Prog Brain Res 83, 161–187. [PubMed: 2203097]

Stuhmer W, Ruppersberg JP, Schroter KH, Sakmann B, Stocker M, Giese KP, Perschke A, Baumann A & Pongs O (1989). Molecular basis of functional diversity of voltage-gated potassium channels in mammalian brain. EMBO J 8, 3235–3244. [PubMed: 2555158]

Suarez-Delgado E, Rangel-Sandin TG, Ishida IG, Rangel-Yescas GE, Rosenbaum T & Islas LD (2020). KV1.2 channels inactivate through a mechanism similar to C-type inactivation. J Gen Physiol, 10.1101/784249

Swartz KJ (2008). Sensing voltage across lipid membranes. Nature 456, 891–897. [PubMed: 19092925]

Syrbe S, Hedrich UBS, Riesch E, Djemie T, Muller S, Moller RS, Maher B, Hernandez-Hernandez L, Synofzik M, Caglayan HS, Arslan M, Serratosa JM, Nothnagel M, May P, Krause R, Loffler H, Detert K, Dorn T, Vogt H, Kramer G, Schols L, Mullis PE, Linnankivi T, Lehesjoki AE, Sterbova K, Craiu DC, Hoffman-Zacharska D, Korff CM, Weber YG, Steinlin M, Gallati S, Bertsche A, Bernhard MK, Merkenschlager A, Kiess W, Euro ERESc, Gonzalez M, Zuchner S, Palotie A, Suls A, De Jonghe P, Helbig I, Biskup S, Wolff M, Maljevic S, Schule R, Sisodiya SM, Weckhuysen S, Lerche H & Lemke JR (2015). De novo loss- or gain-of-function mutations in KCNA2 cause epileptic encephalopathy. Nat Genet 47, 393–399. [PubMed: 25751627]

Taglialatela M, Toro L & Stefani E (1992). Novel voltage clamp to record small, fast currents from ion channels expressed in *Xenopus* oocytes. Biophys J 61, 78–82. [PubMed: 1311612]

Tao X, Lee A, Limapichat W, Dougherty DA & MacKinnon R (2010). A gating charge transfer center in voltage sensors. Science 328, 67–73. [PubMed: 20360102]

Tombola F, Pathak MM & Isacoff EY (2006). How does voltage open an ion channel? Annu Rev Cell Dev Biol 22, 23–52. [PubMed: 16704338]

Trimmer JS (2015). Subcellular localization of K^+ channels in mammalian brain neurons: remarkable precision in the midst of extraordinary complexity. Neuron 85, 238–256. [PubMed: 25611506]

Vacher H, Mohapatra DP & Trimmer JS (2008). Localization and targeting of voltage-dependent ion channels in mammalian central neurons. Physiol Rev 88, 1407–1447. [PubMed: 18923186]

van Veenendaal TM, IJff DM, Aldenkamp AP, Holman PAM, Vlooswijk MCG, Rouhl RPW, de Louw AJ, Backes WH & Jansen JFA (2015). Metabolic and functional MR biomarkers of antiepileptic drug effectiveness: A review. Neurosci Biobehav R 59, 92–99.

Wang H, Kunkel DD, Martin TM, Schwartzkroin PA & Tempel BL (1993). Heteromultimeric K^+ channels in terminal and juxtaparanodal regions of neurons. Nature 365, 75–79. [PubMed: 8361541]

Wolff M, Casse-Perrot C & Dravet C (2006). Severe myoclonic epilepsy of infants (Dravet syndrome): natural history and neuropsychological findings. Epilepsia 47(Suppl 2), 45–48. [PubMed: 17105460]

Xie G, Harrison J, Clapcote SJ, Huang Y, Zhang JY, Wang LY & Roder JC (2010). A new Kv1.2 channelopathy underlying cerebellar ataxia. J Biol Chem 285, 32160–32173. [PubMed: 20696761]

Zagotta WN, Hoshi T & Aldrich RW (1994). Shaker potassium channel gating. III: Evaluation of kinetic models for activation. J Gen Physiol 103, 321–362. [PubMed: 8189208]

Author Manuscript
Author Manuscript
Author Manuscript
Author Manuscript

Key points

- $K_V1.2$ channels, encoded by the *KCNA2* gene, regulate neuronal excitability by conducting K^+ upon depolarization. A new *KCNA2* missense variant was discovered in a patient with epilepsy, causing amino acid substitution F302L at helix S4, in the $K_V1.2$ voltage-sensing domain.

- Immunocytochemistry and flow cytometry showed that F302L does not impair KCNA2 subunit surface trafficking.

- Molecular dynamics simulations indicated that F302L alters the exposure of S4 residues to membrane lipids.

- Voltage clamp fluorometry revealed that the voltage-sensing domain of $K_V1.2$-F302L channels is more sensitive to depolarization. Accordingly, $K_V1.2$-F302L channels opened faster and at more negative potentials; however, they also exhibited enhanced inactivation: that is, F302L causes both gain- and loss-of-function effects. Coexpression of KCNA2-WT and -F302L did not fully rescue these effects.

- The proband's symptoms are more characteristic of patients with loss of *KCNA2* function. Enhanced $K_V1.2$ inactivation could lead to increased synaptic release in excitatory neurons, steering neuronal circuits towards epilepsy.
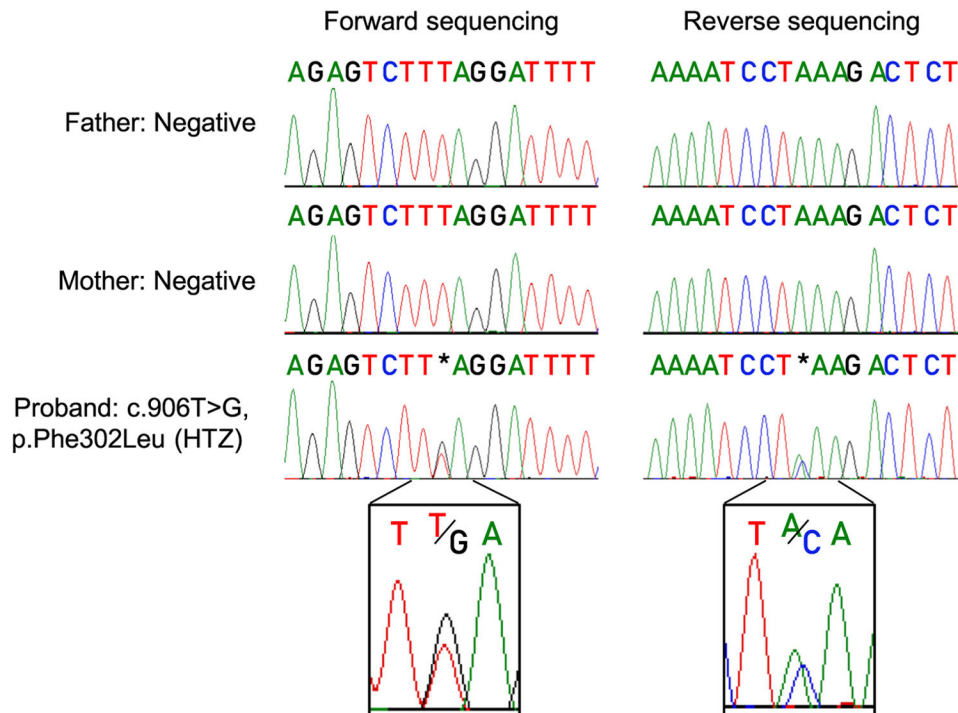
Figure 1. A *de novo* mutation in a conserved *KCNA2* (K$_V$1.2) amino acid from an infant with epilepsy

Sequencing chromatograms of the proband, an infant patient exhibiting epilepsy and her healthy parents. A *de novo* heterozygous (HTZ) mutation 906T>G in *KCNA2*, the gene encoding the pore-forming subunit of K$_V$1.2 channels. The mutation site is indicated by asterisks: two bases, one from each *KCNA2* allele, overlap. Magnified views of the chromatograms are shown in the insets. The missense mutation causes substitution F302L, located in the S4 segment of the K$_V$1.2 voltage-sensing domain (Fig. 2).
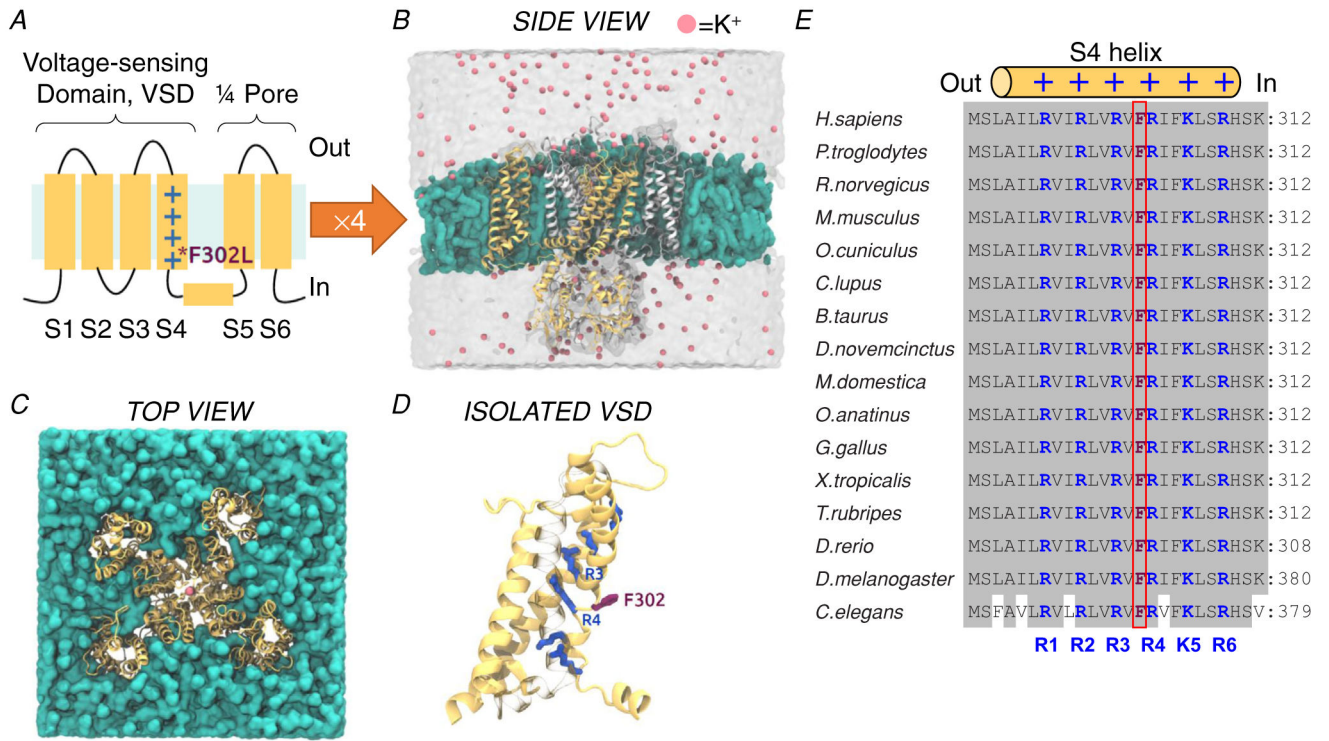
Figure 2. KCNA2 topology and K$_V$1.2 structure

A, cartoon of a K$_V$1.2 subunit. Each rectangle corresponds to a transmembrane helix. Helices S1, S2, S3 and S4 form a voltage-sensing domain (VSD), while helices S5 and S6 from each subunit make up the central, K$^+$-selective pore. The charged residues on S4 are marked with plus symbols, and the location of the mutation F302L is shown with a purple asterisk. *B*, side view of a simulated K$_V$1.2 channel (ribbons) embedded in a membrane (cyan) between the extracellular and intracellular aqueous environment. A single KCNA2 subunit is highlighted in yellow. K$^+$ ions are depicted as pink spheres. *C*, top view of a simulated K$_V$1.2 channel structure (yellow ribbons) embedded in the membrane (cyan). Note the K$^+$ ions (pink spheres) permeating the central pore. *D*, a molecular view of an isolated VSD, where the S4 residues involved in charge transfer (R1–R4; Ishida et al. 2015) are highlighted with blue sticks. F302 is shown with purple sticks. *E*, the S4 helix region (including F302, framed in red) is highly conserved in *KCNA2* across different species, as well as *Shaker*, the archetypal voltage-gated K$^+$ channel from the fruitfly and *shk-1*, the *Caenorhabditis elegans* orthologue. Conserved, positively charged arginine (R) and lysine (K) residues are in blue. The grey background denotes sequence identity.
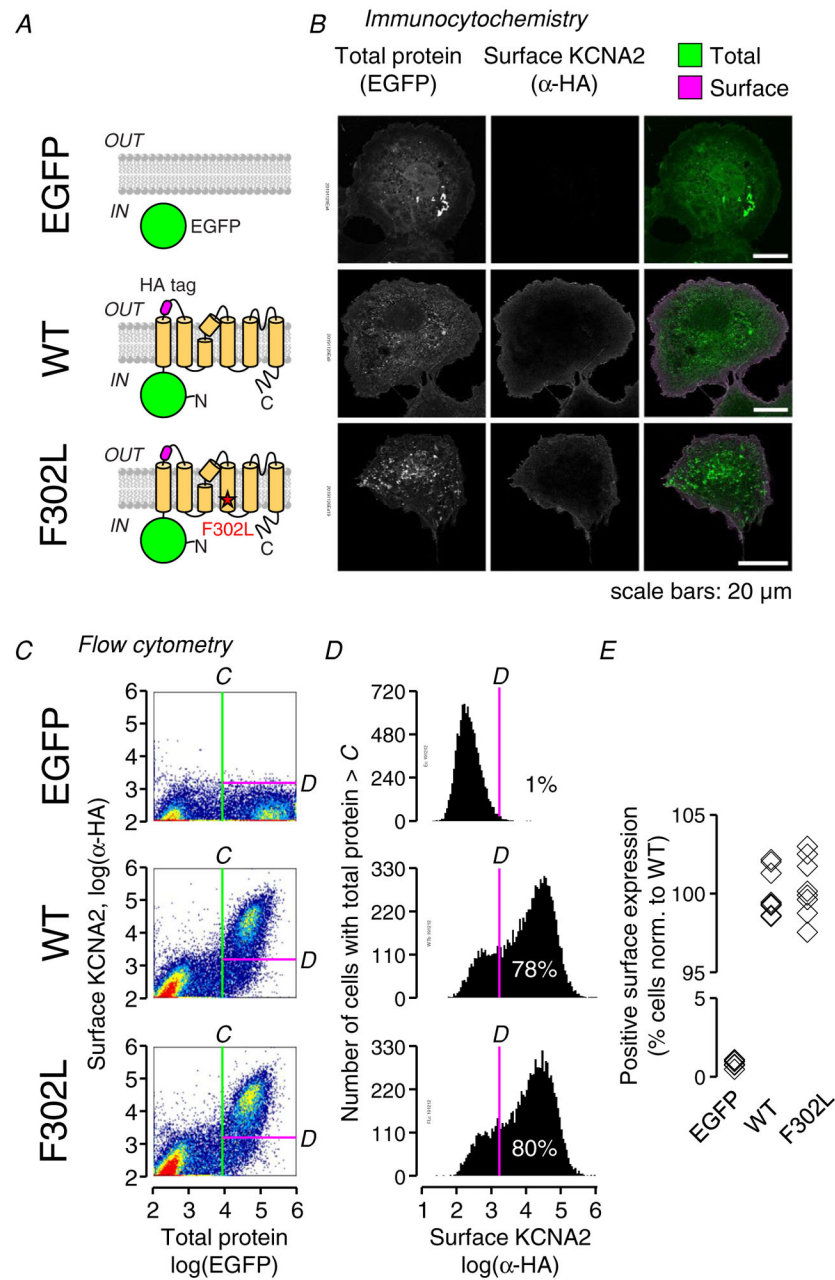
Figure 3. F302L does not affect KCNA2 membrane expression

A, constructs used for evaluating KCNA2 membrane trafficking. Top: EGFP, a non-membrane-associated fluorescent protein. Middle: KCNA2 with N-terminally fused EGFP, reporting total protein production; and a haemagglutinin (HA) tag at the extracellular loop between S1 and S2. In non-permeabilized cells, only KCNA2 subunits at the cell membrane have HA-tags that are accessible to antibody labelling; therefore, HA fluorescence labelling (α-HA) reports surface expression of KCNA2. Bottom: the same EGFP-KCNA2(HA) construct bearing F302L. *B*, exemplary immunocytochemical confocal micrographs of COS-7 cells transiently expressing the constructs in *A*. Left: EGFP signal. Middle: signal from surface-labelled HA (α-HA). Right: merged EGFP (green) and α-HA (magenta)

signals. *C–E*, flow cytometry analysis of live COS-7 cells transiently transfected with the constructs in *A*. *C*, representative cell density plots of total protein (EGFP signal) against surface expression (*a*-HA). The vertical green line (*C*-gate) separates low- and high-EGFP cells (left/right). The horizontal purple line (*D*-gate) separates high-EGFP cells into *a*-HA-negative (bottom) and *a*-HA-positive (top). *D*, cell count distributions with high total protein (EGFP signal) plotted against surface expression (*a*-HA signal). The purple line (*D*-gate, as in *C*) separates cells into *a*-HA-negative (left) and *a*-HA-positive (right). The percentage of *a*-HA-positive cells is shown in the inset. *E*, percentage of surface-expression- (*a*-HA−) positive cells, normalized to cells expressing KCNA2-WT. Mean ± SD: EGFP: $0.69 \pm 0.35\%$ ($n = 7$; where n represents one cell preparation (transfection) containing at least 4000 EGFP-positive cell counts); WT: $100 \pm 1.4\%$ ($n = 9$); F302L: $101 \pm 1.9\%$ ($n = 9$). The *P*-value for KCNA2-F302L and KCNA2-WT was 0.42 (Student's *t* test, unpaired, two-tailed).
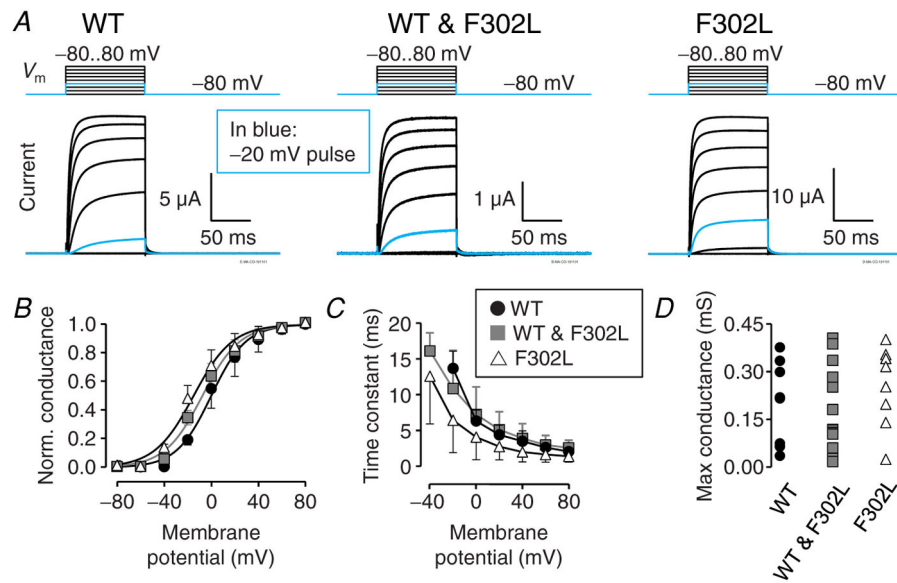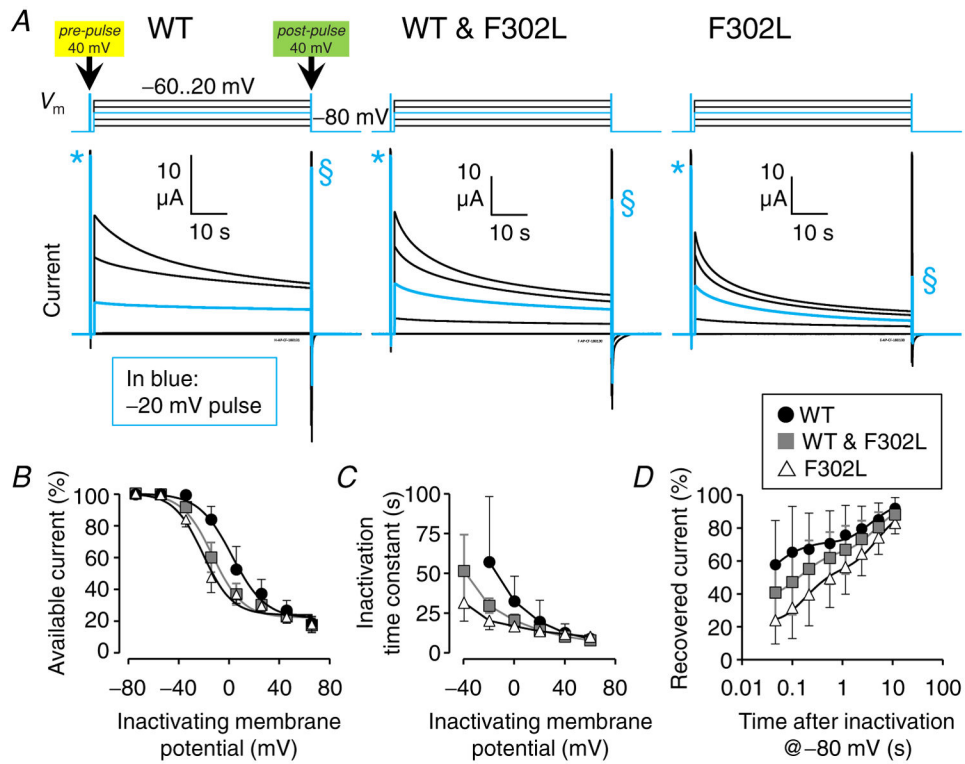
Figure 4. F302L facilitates and accelerates voltage-dependent $K_V1.2$ activation

A, super-imposed voltage protocol and current recorded from $K_V1.2$ channels composed of wild-type (left), coexpressed wild-type and F302L subunits (middle), and F302L subunits (right). Pulse duration was 100 ms. The current recorded in the pulse to −20 mV is shown in blue. *B*, normalized macroscopic conductance of wild-type (circles), wild-type/F302L subunit coexpression (squares) and F302L (triangles) plotted against the test membrane potential. The curves represent fits to Boltzmann distributions (mean ± SD). Wild-type: $V_{0.5} = 1.0 ± 7.3$ mV; $z = 1.9 ± 0.76 \ e^0$; $n = 8$. Wild-type & F302L: $V_{0.5} = −7.1 ± 5.1$ mV; $z = 1.7 ± 0.43 \ e^0$; $n = 15$. F302L: $V_{0.5} = −14 ± 6.7$ mV; $z = 1.7 ± 0.55 \ e^0$; $n = 8$. *C*, weighted activation time constant of wild-type (circles), wild-type/F302L subunit coexpression (squares) and F302L (triangles) plotted against the test membrane potential. *D*, maximal macroscopic $K_V1.2$ conductance (extracted from the fits to Boltzmann distribution; mean ± SD) in oocytes expressing KCNA2-WT ($0.20 ± 0.13$ mS, $n = 8$; circles), KCNA2-F302L ($0.25 ± 0.13$ mS; $n = 8$; $p = 0.44$; triangles), and both KCNA2-WT and -F302L subunits ($0.16 ± 0.14$ mS; $n = 15$; $p = 0.51$; squares). *P*-values were calculated using Student's *t* test (unpaired, two-tailed). In all panels, error bars represent 1 SD.
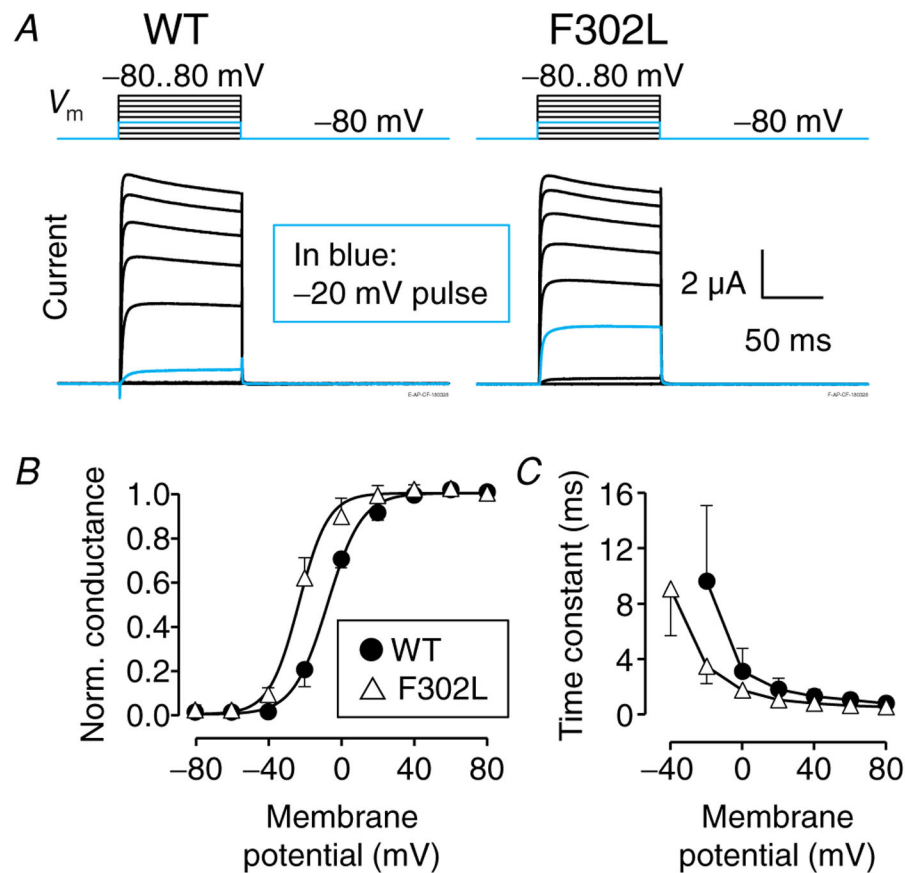
Figure 5. F302L facilitates and accelerates voltage-dependent $K_V1.2$ activation at near-physiological temperature

A, super-imposed voltage protocol and current recorded from wild-type (left) and F302L (right) $K_V1.2$ channels at 33°C. Pulse duration was 100 ms. The current recorded in the pulse to −20 mV is shown in blue. B, normalized macroscopic conductance (recorded at 33°C) of wild-type (circles) and F302L (triangles) $K_V1.2$ plotted against the test membrane potential. The curves represent fits to Boltzmann distributions (mean ± SD). Wild-type: $V_{0.5}$ = −7.4 ± 1.9 mV; $z = 2.9 ± 0.59$ e^0; $n = 6$. F302L: $V_{0.5} = −23 ± 4.1$ mV; $z = 3.2 ± 0.77$ e^0; $n = 7$. C, activation time constant of wild-type (circles) and F302L (triangles) $K_V1.2$ for experiments at 33°C plotted against the test membrane potential. In all panels, error bars represent 1 SD.

Figure 6. F302L facilitates and accelerates voltage-dependent $K_V1.2$ inactivation

A, super-imposed voltage protocol and current recorded from $K_V1.2$ channels composed of wild-type (left), co-expressed wild-type and F302L subunits (middle) and F302L subunits (right). The inactivating pulse duration was 1 min and was flanked by 200-ms pre- and post-pulses to 40 mV. The current recorded with the inactivating pulse to −20 mV is shown in blue. Current elicited by the pre- and post-pulses is marked with * and §, respectively. *B*, non-inactivated current portion (i.e. §/*) of wild-type (circles), wild-type/F302L subunit coexpression (squares) and F302L (triangles) plotted against the inactivation membrane potential. The curves represent fits to Boltzmann distributions (mean ± SD). Wild-type: $V_{0.5}$ = −2.1 ± 10 mV; z = 2.2 ± 0.57 e^0; ped = 20 ± 4.6%; n = 8. Wild-type & F302L: $V_{0.5}$ = −18.1 ± 6.9 mV; z = 2.3 ± 0.53 e^0; ped = 22 ± 4.3%; n = 8. F302L: $V_{0.5}$ = −24.6 ± 7.9 mV; z = 2.4 ± 0.87 e^0; ped = 22 ± 5.3%; n = 8. *C*, onset of inactivation of wild-type (circles), wild-type/F302L subunit coexpression (squares) and F302L (triangles) plotted against the inactivation membrane potential. *D*, recovered current expressed as a fraction of the current available in the pre-pulse, plotted against recovery time at −80 mV. The data were fit to a sum of two exponential functions with a baseline offset (*b*) to account for non-inactivated channel current. WT (circles): τ_1 = 0.02 s (62%); τ_2 = 3.5 s; b = 28%; τ_{avg} = 1.4 s; n = 7. WT & F302L (squares): τ_1 = 0.14 s (50%); τ_2 = 4.7 s; b = 39%; τ_{avg} = 2.5 s; n = 12. F302L (triangles): τ_1 = 0.18 s (49%); τ_2 = 4.7 s; b = 24%; τ_{avg} = 2.8 s; n = 7. In all panels, error bars represent 1 SD.
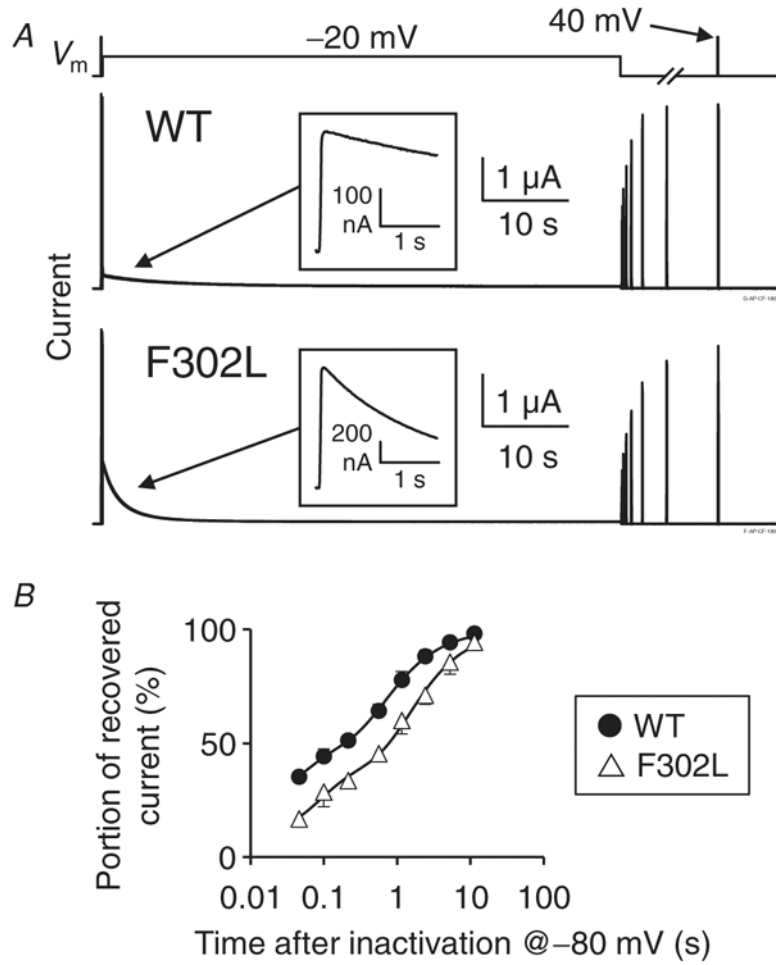
Figure 7. F302L accelerates voltage-dependent $K_V1.2$ inactivation and delays inactivation recovery at near-physiological temperature

A, representative $K_V1.2$ currents recorded during inactivation recovery experiments at 33°C. The protocol consisted of a brief (50 ms) pulse at 40 mV, followed by a 1 min inactivating pulse at −20 mV. The available (recovered) channels were evaluated by brief (50 ms) pulses to 40 mV at approximately half-log time intervals following the inactivating pulse. The protocol cycle period was 5 min. The insets show the first 2 s of the inactivating pulse, to better illustrate that $K_V1.2$-F302L channels inactivate faster than wild-type. *B*, recovered current expressed as a fraction of the current available in the pre-pulse, plotted against recovery time at −80 mV, for experiments at 33°C. The data were fit to a sum of two exponential functions with a baseline offset (*b*) to account for non-inactivated channel current. WT (circles): $\tau_1 = 0.06$ s (41%); $\tau_2 = 0.77$ s; $b = 27\%$; $\tau_{avg} = 0.48$ s; $n = 5$. F302L (triangles): $\tau_1 = 0.09$ s (40%); $\tau_2 = 1.6$ s; $b = 12\%$; $\tau_{avg} = 1.0$ s; $n = 7$. Error bars represent 1 SD.
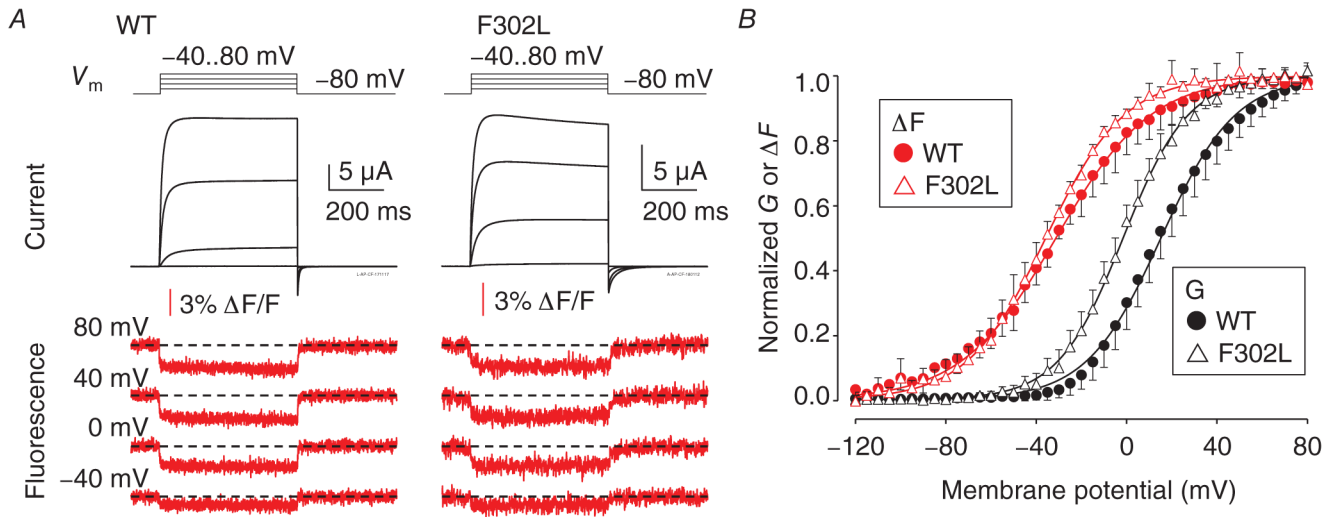
**Figure 8. F302L facilitates activation of the $K_V1.2$ VSDs**

A, super-imposed voltage protocol and current (black) recorded from $K_V1.2$ channels fluorescently labelled at the S4 segment with (right) or without (left) mutation F302L. Simultaneously acquired fluorescence deflections (F), reflecting VSD voltage-evoked activation transitions, are shown below (red). *B*, normalized macroscopic conductance (*G*) of fluorescently labelled $K_V1.2$ channels (WT: black circles; F302L: black triangles) and VSD activation (F; WT: red circles; F302L: red triangles). The curves represent fits to Boltzmann distributions (mean ± SD). Wild-type *G*: $V_{0.5} = 15 \pm 6.5$ mV; $z = 1.6 \pm 0.15$ e_0; F: $V_{0.5} = -32 \pm 3.9$ mV; $z = 1.2 \pm 0.32$ e_0; $n = 7$ oocytes. F302L *G*: $V_{0.5} = -1.5 \pm 3.85$ mV; $z = 1.8 \pm 0.32$ e_0; F: $V_{0.5} = -36 \pm 2.6$ mV; $z = 1.5 \pm 0.23$ e_0; $n = 6$ oocytes. Error bars represent 1 SD.
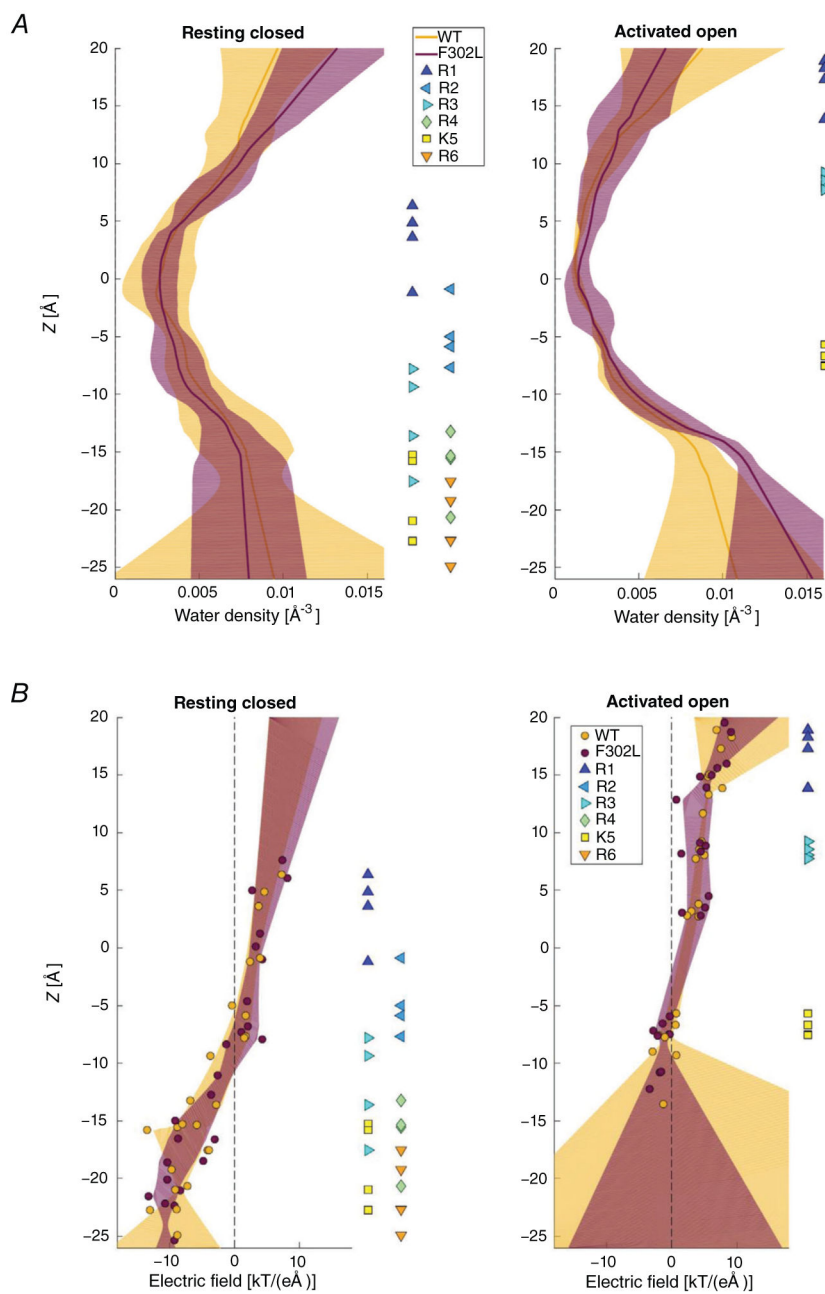
Figure 9. F302L does not alter the water permeation or electric field properties of the $K_V1.2$ VSD

Water density (*A*) and electric field (*B*) along the *Z*-direction in the VSD of WT (orange) or F302L channels (plum) are shown for the resting-closed (left) and activated-open (right) states. The position (*Z* value) of positively charged residues on S4 of each subunit is marked with coloured symbols located on the right of the plots.
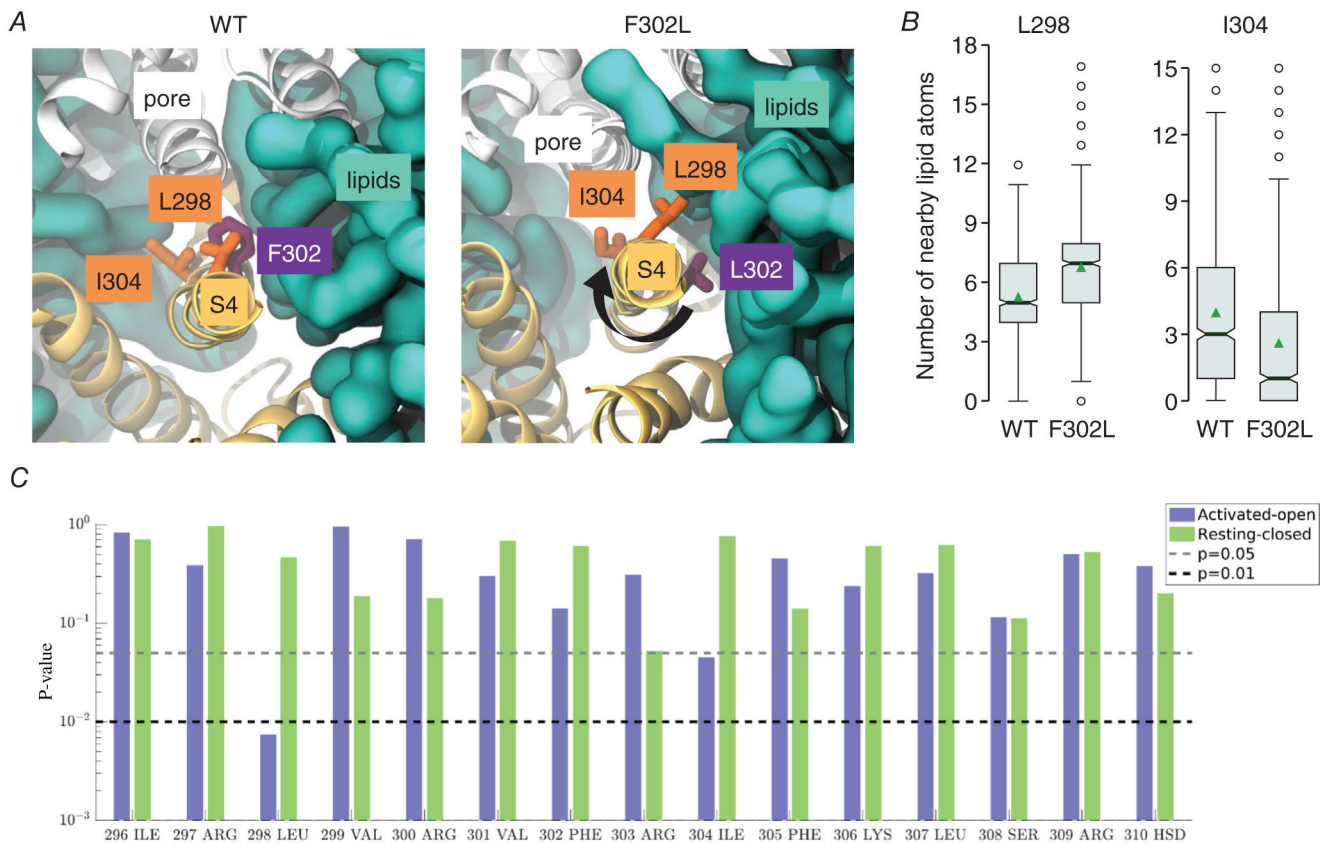
Figure 10. F302L alters the local environment of S4 helix

A, top views of the S4 helix in the AO conformation of a WT VSD (left) and one with F302L (right). S4 and other VSD helices are rendered in yellow; pore domain helices in white; membrane lipids in cyan. The side-chains of residues L298 and I304 are shown in orange; F302 (left) and L302 (right) are shown in purple. Note (i) the altered lipid interaction of L298 and I304 with membrane lipids, and (ii) the slight rotation of S4 (black arrow), indicating a change in membrane lipid exposure. *B*, box-and-whiskers plots of nearby (within 4.5 Å) lipid atom counts for residues L298 and I304, on the S4 helix, in the active VSD and open pore conformation of WT or F302L channels. Green triangle: mean; heavy bar/notch: median; box: interquartile range (IQR); whisker bounds: Q1–1.5 × IQR and Q3+1.5 × IQR; circles: outlying observations. For both residues, $P < 0.05$. *C*, P-values for the number of nearby lipid atoms (F302L *vs.* WT) for all S4 residues.
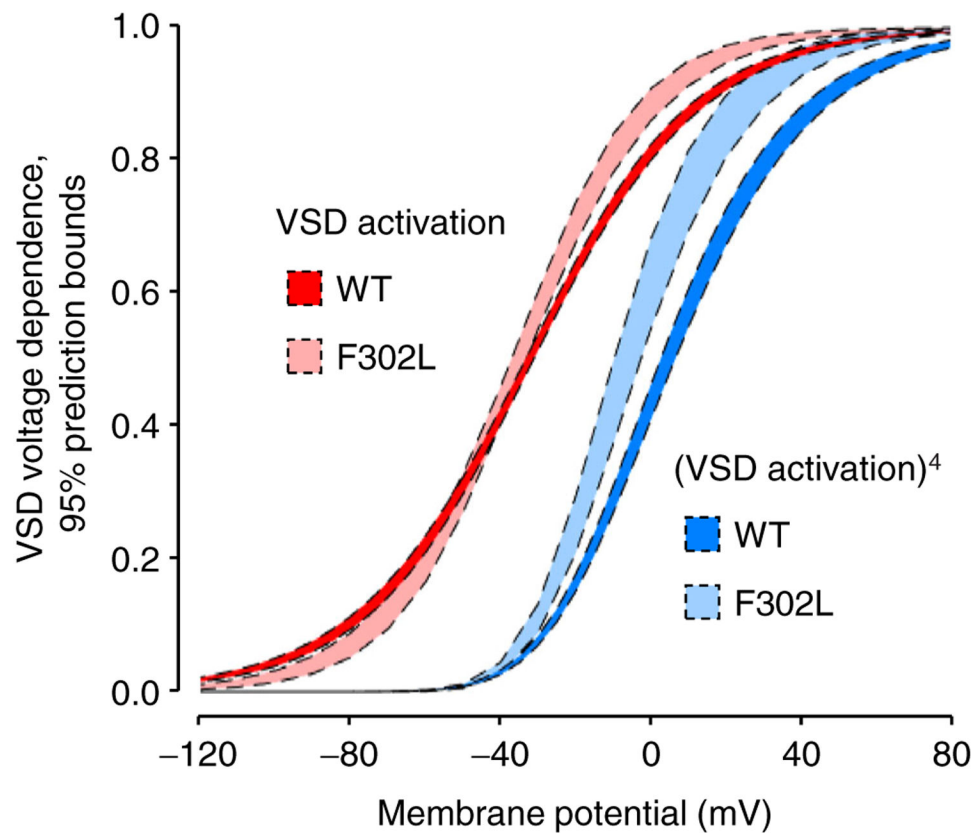
Figure 11. The modest effect of F302L on the voltage dependence of $K_V1.2$ VSD activation is sufficient to account for a larger shift in the voltage dependence of channel opening

The 95% prediction bounds for VSD activation probability in WT (red) or F302L (pink) channels, from voltage clamp fluorometry data as in Fig. 8B. Mean and 95% confidence interval for the Boltzmann fitting parameters: WT: $V_{0.5} = -32.4$ [$-31.5, -33.2$] mV, $z = 1.15$ [1.11, 1.19] e^0; F302L: $V_{0.5} = -35.2$ [$-33.7, -36.8$] mV, $z = 1.46$ [1.34, 1.58] e^0. Assuming that four $K_V1.2$ VSDs are required to activate before the pore can open, the opening probability can be approximated by the fourth power of VSD activation probability. The 95% prediction intervals of WT and F302L VSD activation raised to the fourth power are also plotted, in dark and light blue, respectively. The half-activation potentials of these curves are separated by ~10 mV, consistent with the ~15 mV shift of the macroscopic conductance (Fig. 4B).
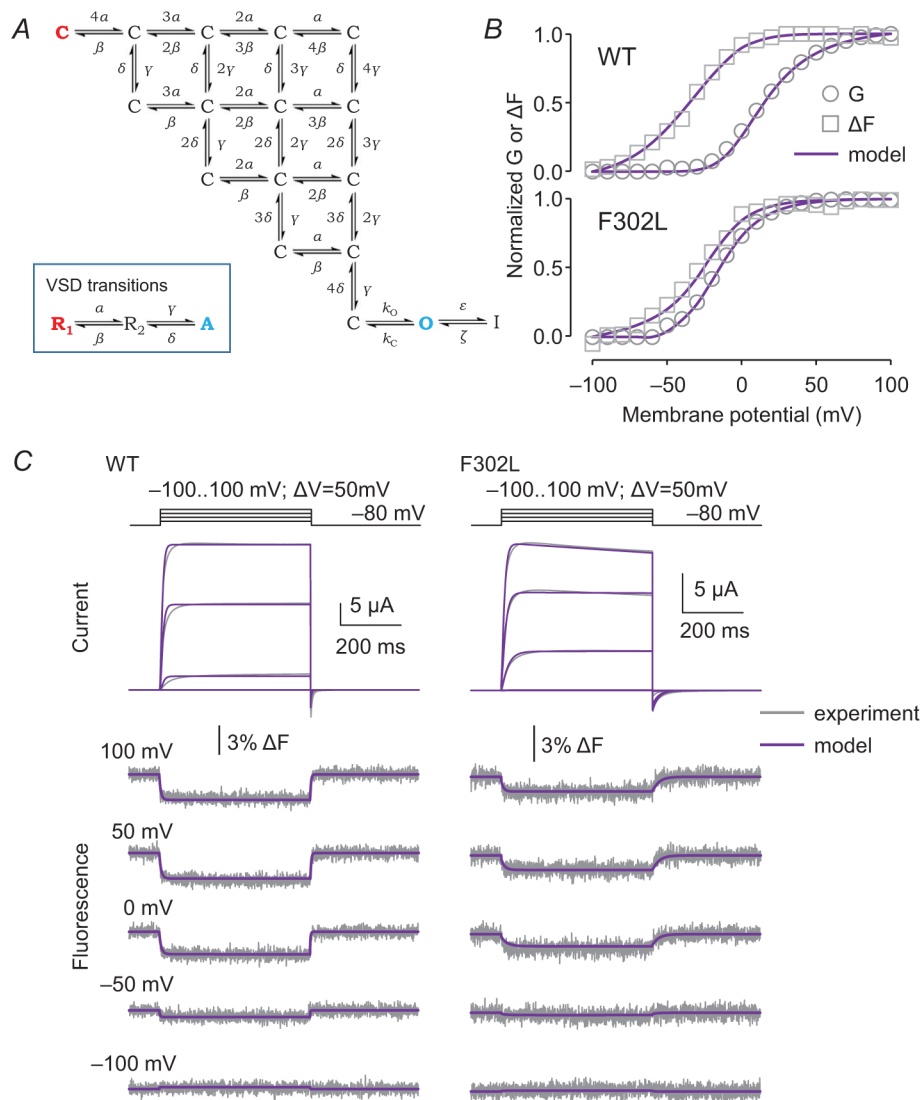
Figure 12. Markov model fitting of voltage-dependent K$_V$1.2-WT and -F302L activation

A, a Markov state-scheme mechanism with 17 states. Each of the four VSDs can undergo two activation transitions, giving rise to 15 closed (C) states. Once all four VSDs are in the fully activated (A) state, the channel may transition to the open (O) state. From the O state, the channel can transition to a closed, inactivated (I) state. The states marked in red (fully resting R$_1$ VSD state and closed channel with four fully resting VSDs C state) and blue (fully activated A VSD state and open channel with four fully activated VSDs O state) were structurally modelled and simulated using MD in this work (RC and AO models, respectively). Model fits are shown in *B* (steady-state, normalized conductance, *G*, or fluorescence changes, *F*) and *C* (representative current and fluorometry traces). Fit data, from the cell in Fig. 8A, are in grey; model outputs in purple. Either WT or F302L datasets included current and fluorescence traces from pulses from −120 mV to 100 mV in 10 mV increments. Model parameters are in Table 1.

Table 1.

$K_V1.2$ model parameters. $K_V1.2$-WT and -F302L Markov voltage-dependent model parameters (Fig. 12). The charge for the opening and closing transitions (C↔O; marked with *) were fixed to 0. As there was very little slow inactivation in the traces, especially in wild-type, inactivation parameters (§) were very poorly determined

Transition or equilibrium	Parameter	WT	F302L
α (R$_1$→R$_2$)	k_α (s^{-1})	150	110
	z_α (e_0)	0.066	0.085
β (R$_1$←R$_2$)	k_β (s^{-1})	44	110
	z_β (e_0)	0.99	9.0E−3
$E_{R1↔R2}$ (0 mV)	**k_α/k_β**	**3.3**	**0.96**
γ (R$_2$→A)	k_γ (s^{-1})	6.8E5	2.6E6
	z_γ (e_0)	0.0024	0.059
δ (R$_2$←A)	k_δ (s^{-1})	7.2E5	1.6E6
	z_δ (e_0)	0.60	0.58
$E_{R2↔A}$ (0 mV)	**k_γ/k_δ**	**0.95**	**1.7**
Pore opening	k_O (s^{-1})	3500	2900
	z_O (e_0)*	0	0
Pore closing	k_C (s^{-1})	390	52
	z_C (e_0)*	0	0
$E_{C↔O}$ (0 mV)	**k_O/k_C**	**8.9**	**58**
Inactivation§	k_ε (s^{-1})	0.0015	1.23
	z_ε (e_0)	0.97	1.8
Inactivation recovery§	k_ζ (s^{-1})	4.1E−7	1.7E−3
	z_ζ (e_0)	0.30	1.1
$E_{O→I}$ (0 mV)§	k_ε/k_ζ	3.5E4	7.4E2
Contribution to F	φ_1	−1.5	−0.30
	φ_2	0	−0.24
Maximal conductance	G (mS)	0.25	0.12

Transition or equilibrium	Parameter	WT	F302L
K^+ reversal potential	E_K (mV)	−59	−58